Laser Photonics Rev. **6**, No. 5, 589–606 (2012) / **DOI** 10.1002/lpor.201000035

LASER & PHOTONICS REVIEWS

Abstract Elementary scattering processes in solid matter occur on ultrafast timescales and photoelectron spectroscopy in the time domain represents an excellent tool for their analysis. Conventional photoemission accesses binding energies of electronic states and their momentum dispersion. The use of femtosecond laser pulses in pump-probe experiments allows obtaining direct insights to the energy and momentum dependence of ultrafast dynamics. This article introduces the elementary interaction processes and emphasizes recent work performed in this rapidly developing field. Decay processes in the low excitation limit are addressed, where electrons decay according to their interaction with carriers in equilibrium. Here, hot electron relaxation in epitaxial metallic film is reviewed. In the limit of an intense optical excitation, scattering of the excited electrons among each other establishes a non-equilibrium state. Results on charge-density wave materials and the effect of coherent nuclear motion on the electronic structure, which can break low symmetry ground states, are discussed. Figure reprinted with permission from [71].

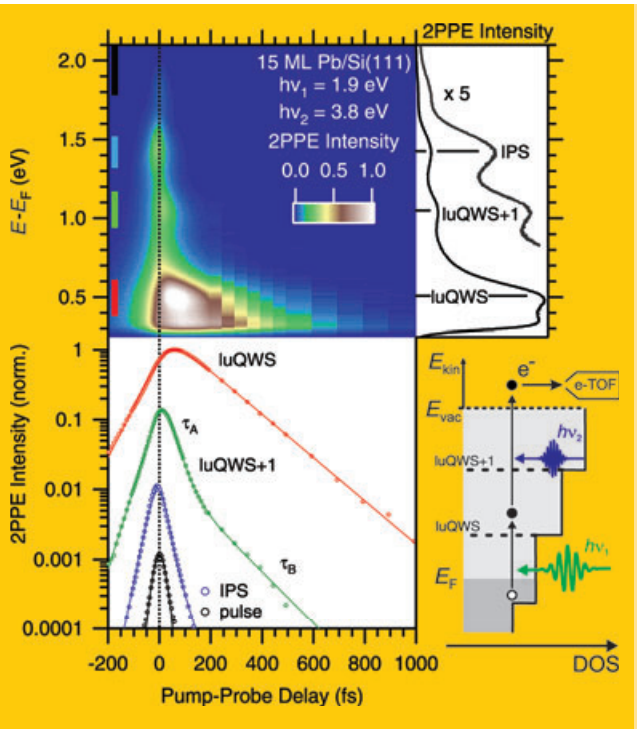

REVIEW ARTICLE

Elementary relaxation processes investigated by femtosecond photoelectron spectroscopy of two-dimensional materials

Uwe Bovensiepen[1,*], **Patrick S. Kirchmann**[2,3]

1. Introduction

The electronic band structure of materials determines the electronic properties like the charge carrier mobility, the effective mass, and the orbital character of the valence and conduction bands. In the last decades angle-resolved photoelectron spectroscopy (ARPES) using photons in the VUV and XUV spectral range has been developed from a surface science method into a complete experimental tool, which provides detailed information on the electronic band structure [1, 2]. Gas discharge lamps and synchrotron light sources are widely employed to generate the required photons. Also lasers [3,4] and laser driven high harmonic (HHG) light sources [5–11] have been established as complementary tools which provide either excellent energy resolution down to several 100 μeV [4] or time resolution down to the attosecond regime [7].

Conventional photoelectron spectroscopy is carried out in the frequency domain, which serves as a reliable determination of transition or binding energies E representing the real part of the spectral function. The line width of the spectroscopic line under study, i. e. the respective imaginary part, provides information on the decay rate Γ, at which the population of a state decays. A first estimate of Γ can be obtained from the electronic relaxation time τ introduced by Drude as a microscopic description of the electrical conductivity σ with $\sigma \propto \tau$ [12]. A description of the measured electrical conductivity of typical metals requires τ to be in the order of several hundred femtoseconds ($1\,\mathrm{fs} = 10^{-15}\mathrm{s}$). The microscopic mechanism proposed by Drude, which explains the electrical resistivity by scattering of electrons with ion cores, is, however, by far too simple. Nevertheless, the order of magnitude of τ demonstrates that elementary scattering rates range typically from 10^{12}–$10^{15}\ \mathrm{s}^{-1}$.

[1] Universität Duisburg-Essen, Fakultät für Physik, Lotharstr. 1, 47048 Duisburg, Germany
[2] Stanford Institute for Materials and Energy Science, 476 Lomita Mall, Stanford, CA 94305, USA
[3] Fritz-Haber-Institut der Max-Planck-Gesellschaft, Physikalische Chemie, Faradayweg 4–6, 14195 Berlin, Germany
[*] Corresponding author: e-mail: uwe.bovensiepen@uni-due.de

In condensed matter various elementary interaction processes contribute to the decay. Following Matthiesen's rule the rates of the individual processes Γ_i add up to the total decay rate $\Gamma = \sum_i \Gamma_i$. As an example consider a hot electron above the Fermi level E_F. It can decay by interaction with other electrons, with phonons, or spin waves (magnons) with respective decay rates $\Gamma_{e\text{-}e}$, $\Gamma_{e\text{-}ph}$, and $\Gamma_{e\text{-}m}$. A microscopic understanding of these processes and which one of them dominates under particular conditions is one of the current challenges in the field. Figure 1 gives an overview of various processes and the typically covered line width range (top axis). The bottom axis provides the relaxation time $\tau = \hbar/\Gamma$ that corresponds to the line width. Here, an earlier, seminal version of this figure is adopted from [13] for a broader discussion of the relevant elementary processes.

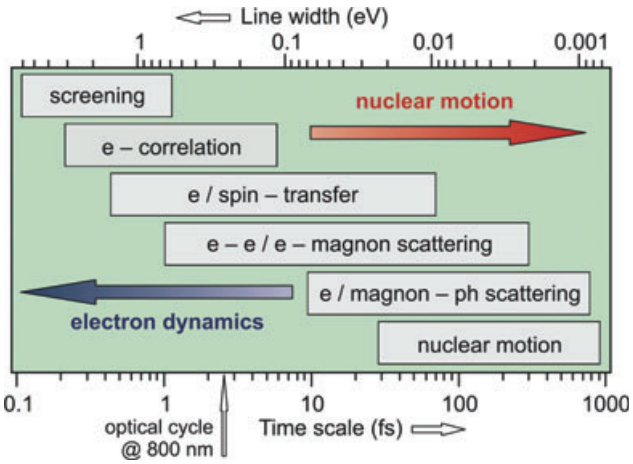

Figure 1 (online color at: www.lpr-journal.org) Typical time scales and respective line widths of elementary excitations and decay processes in solid materials. While the various electronic processes cover the full sub-picosecond range and reach far into the attosecond range, dephasing and decay of ion core vibration is limited to timescales faster than several 10 fs dependent on the atomic mass; modified from [13].

Decay and dephasing of nuclear motion like vibrational wave packet propagation in molecules [14, 15] or coherent optical phonon dynamics in condensed matter range from few 10 fs [16] in light molecules to several ps in inorganic systems with heavier nuclei [17]. Scattering of electrons or magnons with phonons is responsible for energy transfer between different degrees of freedom in a solid. Characteristic times cover a wide range from ps up to few 10 fs in strongly coupled systems [18–21]. Electron-electron (e-e) scattering, which in ferromagnets can be accompanied by magnon excitation [22–24], represents a major energy decay channel of excited electrons. The respective relaxation times have been widely studied in experiment and theory [25, 26] and range from several fs up to several 100 fs.

Transfer of an electron or its spin across interfaces is an essential relaxation process in two-dimensional systems supported by a substrate. Excess energy is transported along a spatial coordinate to a different point in space, where it can decay subsequently. In particular at interfaces local energy decay and transfer processes compete in many situations. The current state of this field is presented in [27].

Let us consider a simple example to emphasize the ultrafast time scale in a two-dimensional system. Spreading of an electron wave packet from a free electron like metallic surface into the bulk can be viewed as the ultrafast limit of electron transfer. The characteristic time of wave packet spreading is set by the initial localization and reaches well into the sub-femtosecond scale, as found for wave packets localized to individual atoms adsorbed on a surface [25, 28]. In the free electron limit the momentum band width, which is required to form this wave packet from free electron like states, forces the wave packet to spread with a characteristic time proportional to the square of the wave packet's diameter [29]. In case of localization to a rather heavy atom with a diameter of 5 Å this gives a spreading time of 2.5 fs. For weaker electronic coupling these transfer times slow down. In molecular systems charge transfer is mediated by molecular rearrangement [30], which can become a rather slow process at low temperatures since it is assisted by nuclear motion.

Figure 1 mentions two further points in the time range of femto- and attoseconds. One aspect is related to electron correlation which addresses electronic many body effects related to the e-e interaction described by an energy U. In so-called Mott-insulators mutual repelling of electrons leads to an insulating state. The fluctuations of this state occur at a characteristic time scale of $\hbar/W \approx 1$ fs; W is given by the electronic band width [31]. Finally, screening in systems with high electron density is considered. Here, formation of an excess charge or hole is screened by the electron density as a whole, which responds collectively at frequencies up to the plasma frequency, i. e. in the attosecond range [32].

Summarizing this introduction we note that dynamics due to nuclear motion exhibit characteristic timescales from the pico- to the femtosecond range, where the fast limit is given by vibrational frequencies of light ion cores. Electron dynamics reach from femtoseconds far into the attosecond scale. Here the fast limit is set by the collective response time of the charge density.

Analysis of these processes and their competition is challenging. Photoelectron spectroscopy performed in the frequency domain at surfaces provides important information to disentangle e-e-, electron-phonon- (e-ph), and electron-impurity scattering through line width analysis [33–35]. Photoelectron spectroscopy in the time domain provides a versatile, complementary tool. The duration of an optical cycle of the fundamental emission of Ti:Sapphire lasers in the vicinity of 800 nm is with 2.7 fs considerably shorter than various processes of interest discussed here. Therefore, the use of femtosecond laser pulses, which are nowadays routinely available in a broad wavelength range with pulse durations of few 10 fs, has led to microscopic insight into electronic scattering and interaction processes [13,27,36,37]. These time-domain results are obtained by pump-probe experiments because direct detection schemes are too slow to detect the ultrafast processes.

The present review article aims at an audience which is familiar with the currently available femtosecond laser

technology and is interested in the current state of the art of photoemission experiments in the time domain. In particular, the understanding of ultrafast electron dynamics obtained for a number of surface problems [13, 36, 37] is extended to two-dimensional material systems. With this aim we discuss selected examples of femtosecond electron dynamics investigated by time-resolved photoelectron spectroscopy for metallic films. In addition, exemplary charge density wave materials are discussed as examples for ultrafast dynamics of systems exhibiting cooperative phenomena. Moreover, we pay attention to the aspect of the optical excitation density in the pump-probe experiments. We start with experimental aspects (Sect. 2) and proceed with the weak excitation regime were the excited charge carriers can be considered to not interact with each other, see Sect. 3. Relaxation in this regime is termed few particle dynamics. For higher excitation density excited carriers scatter among each other and the decay proceeds in the limit of many particle dynamics, which is the topic of Sect. 4. Finally, we summarize and conclude the article in Sect. 5 with a brief outlook on current challenges.

2. Experimental aspects

In order to provide a sufficiently large mean free path for photoelectrons to propagate from the sample to the electron spectrometer experiments are carried out under vacuum. Since, furthermore, photoelectron spectroscopy is a surface sensitive technique vacuum conditions which facilitate a control of the surface composition are required. These are achieved by the help of ultrahigh vacuum (UHV) with a base pressure of 10^{-10} mbar or better.

Photoelectrons propagate from the sample surface to spectrometer through vacuum as free electrons. In the present context they are emitted from solid surfaces and can be characterized by their kinetic energy E_{kin} and their momentum component parallel to the surface $k_{||}$ [1, 2, 5]. Here we consider generation of photoelectrons by absorption of photons in the ultraviolet (UV) and visible (VIS) spectral range. It is useful to distinguish linear and non-linear photoelectron emission. For photon energies $h\nu$ larger than the work function $\Phi = E_{\mathrm{vac}} - E_{\mathrm{F}}$, where E_{vac} is the vacuum level of the surface and E_{F} is the Fermi level, absorption of one photon is required for such a direct photoemission event. For $h\nu < \Phi$ absorption of two photons can lead to photoemission. This process is referred to as two-photon photoemission (2PPE) [38]. Both processes are illustrated in Fig. 2. If excited by ultrashort laser pulses both schemes can be employed in pump-probe experiments to study ultrafast processes. However, they provide information about essentially different relaxation dynamics. In time-resolved 2PPE the population decay of a state at energy E_{i} and a momentum $k_{||}$ is probed. The optical excitation density F employed here is $F = 1$–$10\,\mu\mathrm{J/cm}^2$. Note that it depends on the sequence of the laser pulses whether states close to E_{vac} or close to E_{F} are excited if a combination of UV and VIS pulses are used for pump and probe studies, see Fig. 2, top. Similarly, two UV pulses, which are delayed with respect to each other,

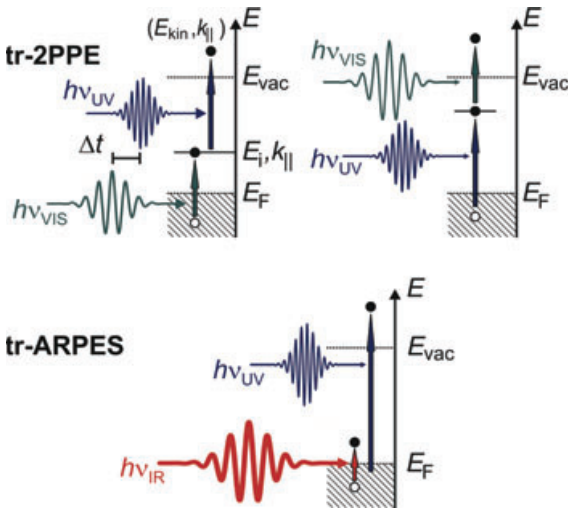

Figure 2 (online color at: www.lpr-journal.org) Time-resolved non-linear and linear photoemission schemes: At top two-color two-photon photoemission (2PPE) is depicted for the case of VIS pump and UV probe (left) and vice versa (right). Here the UV photon energy $h\nu_{\mathrm{UV}} < E_{\mathrm{vac}} - E_{\mathrm{F}}$. The detected photoelectrons are analyzed with respect to their kinetic energy E_{kin} and momentum component parallel to surface $k_{||}$ in an electron spectrometer. The bottom panel indicates a time-resolved linear photoemission scheme in which the sample under investigation is pumped by an IR and probed by a UV or VUV pulse with a photon energy $h\nu_{\mathrm{UV}} > E_{\mathrm{vac}} - E_{\mathrm{F}}$.

can be employed for 2PPE [13]. In the direct photoemission pump-probe scheme occupied states are analyzed (Fig. 2, bottom). Due to the high yield of direct photoemission without optical excitation a detectable pump-induced change typically requires a higher excitation density than in 2PPE. Therefore effects that occur at these more intense excitation conditions on the order of $F = 0.1 - 1\,\mathrm{mJ/cm}^2$ are tested. However, in principle relaxation of hot holes should be accessible at the lower excitation densities employed in 2PPE. The limitation here is the finite signal to noise ratio. State-of-the-art setups are able of routinely achieving up to 10^5 signal-to-noise ratio.

As pulsed light sources Ti:sapphire lasers are widely used. In our own laboratory we used a commercial tuneable Ti:sapphire laser system, which is based on the regenerative amplifier RegA 9050 manufactured by Coherent. The beam paths of our setup and the obtained typical pulse parameters are given in Fig. 3, top. Regarding the results presented here, we emphasize the tuneable high repetition rate of this laser system up to 300 kHz and stable cw solid state pump lasers. Both are essential to obtain the high signal to noise ratio our conclusions are based on. Alternatively, Ti:sapphire based oscillator system with pulse energies in the ~ 10 nJ range and 80 MHz repetition rate are used in 2PPE experiments [13, 36, 39]. Such laser systems, however, provide limited tunability and rather low energy per pulse. More recently, HHG sources [5–11] enabled generating ultrashort pulses with several 10 eV photon energy. This approach overcomes problems of lower probe photon energies such as

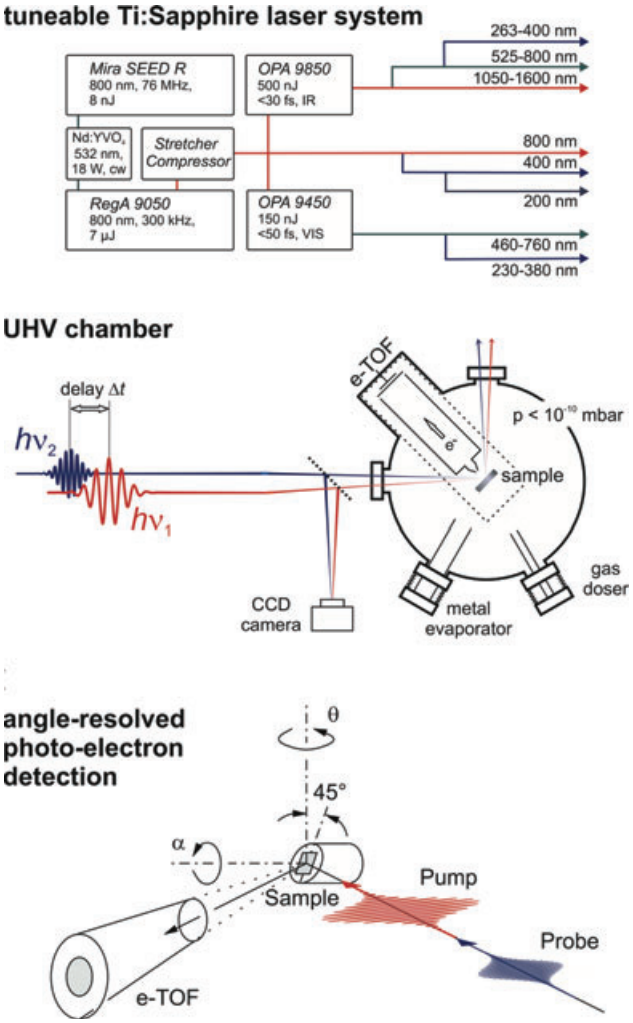

Figure 3 (online color at: www.lpr-journal.org) The experimental setup of our own time-resolved photoelectron spectroscopy from surfaces and interfaces combines a tuneable Ti:Sapphire laser system operating at several 100 kHz repetition rate (top panel) and an ultrahigh vacuum (UHV) chamber (center panel). The laser system is based on a cw-pumped regenerative amplifier (Coherent RegA 9050). Tuning from the near IR into the UV is facilitated by the use of optical parametric amplifiers (Coherent OPA 9450 / 9850). Their respective signal outputs are doubled / quadrupled in non-linear optical crystals. The fundamental output of the amplifier can be frequency doubled and quadrupled as well. The UHV chamber, in which samples are prepared *in situ*, contains the electron time-of-flight spectrometer (e-TOF) and various surface science preparation and characterization tools like evaporators, gas dosers, Auger electron spectrometer, and an instrument for imaging diffraction patterns of low energy electrons. Spatial overlap of pump and probe pulses is verified using a CCD camera positioned outside the vacuum chamber. The bottom panel depicts the sample holder employed in angle-resolved studies. The sample is rotated in front of the spectrometer tube to detect the angular dependence along two independent angles α and θ. The sample can be mounted on a slanted sample post to address a particular point in momentum space. The sample is cooled by a liquid He cryostat onto which the sample holder assembly is mounted.

limited access to the Brillouin zone and poor photoemission cross section for certain materials. The repetition rate of few kHz imposes, however, limits in the dynamical range of the recorded spectra.

Pairs of pump and probe laser pulses are selected for a specific experiment and focused into the UHV chamber onto the sample surface. As an example the two-color 2PPE setup at the Freie Universität Berlin is depicted in Fig. 3, center panel. Our UHV chamber is an example of an ultrafast surface science spectroscopy experiment being equipped with various tools for film preparation and characterization like gas dosers, metal evaporators, Auger electron spectrometer, and optics for low energy electron diffraction. For photoelectron analysis we employ a time of flight spectrometer optimized for detection of low energy electrons emitted by laser pulses, whose typical kinetic energies are < 2 eV. The acceptance angle of our electron time-of-flight spectrometer is $\pm 3^\circ$, which enables angle-resolved studies due to the low kinetic energy according to $k_{||} = \sin\theta \cdot \sqrt{E_{\mathrm{kin}}/2m}$, θ is the photoemission angle with respect to the surface normal. For certain experiments it is important to access a particular point in momentum space, which can be achieved up to a certain limit by mounting the sample on a slanted sample post in combination with a variation of the azimuthal angle α. See Fig. 3, bottom panel, for an illustration. Other approaches use electrostatic hemispherical electron analyzers [11, 13, 36, 40–42], which can, when used in imaging configurations, enhance the efficiency of angle-resolved photoelectron detection. A combination with the use of VUV photon energies facilitates time- and momentum-resolved access to the full Brillouin zone.

3. Few particle dynamics of hot electron decay in epitaxial metallic films

We start the discussion of electron quasiparticle dynamics investigated by time-resolved photoemission experiments with a regime in which the number of excited quasiparticles is negligible compared to the total number of quasiparticles. The distribution functions of the sample under study remain essentially unchanged compared to the thermal equilibrium prior to the optical excitation. In the relaxation process of the excited state a rather small number of individual quasiparticles, i. e. few, have to be taken into account.

In metals absorption of a photon generates an electron-hole pair. The large electron density results in an efficient and extremely fast screening of the photohole [32, 43–45]. Exciton formation does not occur and the decay of the excited (or hot) electron can be studied directly in the time domain.

If we consider hot electron energies of $0.1 - 1$ eV, which are larger than typical phonon energies, the decay is dominated by e-e scattering [25, 35] as described by Fermi liquid theory (FLT). In the limit of a weakly interacting electron liquid with constant density of states in the vicinity of E_{F} the relaxation time $\tau_{\mathrm{e\text{-}e}}$ of hot electrons at an energy $E_{\mathrm{i}} - E_{\mathrm{F}}$ is given by $\tau_{\mathrm{e\text{-}e}} = a \cdot (E_{\mathrm{i}} - E_{\mathrm{F}})^{-2}$. The constant a is determined by the electron density n and accounts for

the strength of the screened Coulomb interaction responsible for e-e scattering and the density of states. The factor $(E_i - E_F)^{-2}$ describes the phase space increase for e-e scattering as an electron at a higher energy has more states to scatter into. To fulfill energy and momentum conservation a second electron must be excited above E_F simultaneously and $\tau_{e\text{-}e} \propto (E_i - E_F)^{-2}$ [46–48]. Transport from the sample surface, where the electrons are probed in 2PPE, into the bulk is an important relaxation channel for these hot electrons [49], which competes with e-e scattering.

In the following we discuss several examples of metallic films grown on metallic and semiconducting substrates. These results demonstrate how these two relaxation channels are separated in the experiment which then allows a discussion of their energy dependence.

3.1. Cu/Si(111)

We start with epitaxial Cu(111) films on Si(111) as function of film thickness to analyze e-e scattering in the metal film itself and the electron transport across the metal-semiconductor interface. The Si substrate presents a global band gap at all electron momenta. Since electron transport across the interface is suppressed for energies within the Si band gap, one might expect a situation where the electron dynamics in the metal film can be decoupled from the substrate.

Copper was evaporated *in situ* onto Si(111) with a film thickness up to 44 nm in order to prepare epitaxial Cu(111) films [50]. Exemplary 2PPE spectra are shown in the inset of the top panel in Fig. 4 for selected time delays between pump and probe pulses. The three peaks observed for the spectrum at 0 fs represent the series of image potential states (IPS) localized in front of the surface and the Shockley surface state (SS) [38]. With increasing pump-probe delay we find a variation in intensity which is shown in the top panel of Fig. 4. At later delays the intensity is described well by a single exponential decay as indicated by the fit (blue line) of the intensity at $E - E_F = 0.3$ eV. At delays close to time zero the behavior is more involved because the decay of electrons from higher energies generate secondary electrons that are responsible for the intensity increase after the pump pulse is over [51]. This explanation is supported by the fact that this delayed intensity increase is more pronounced for energies closer to E_F. An analysis of decay times is still possible as we essentially analyze the decay of the most energetic electrons at that particular delay interval.

The decay times found by this fitting analysis are plotted in Fig. 4, bottom panel, as a function of energy. As expected, the relaxation times increase monotonously for smaller energies in agreement with earlier studies of noble metals [51, 52]. In addition, a considerable variation is found with film thickness d albeit at the investigated thicknesses variations of the electronic structure with film thickness can be neglected. The observed changes are explained by a modification of transport effects with d because the shortest relaxation times are found for a bulk Cu(111) single crystal and the longest times for the thinnest Cu film.

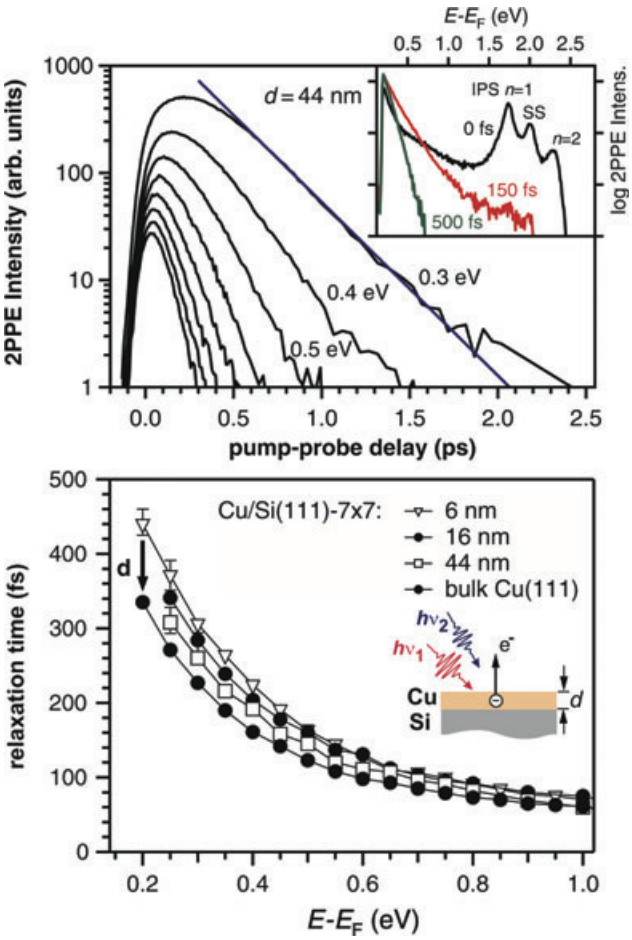

Figure 4 (online color at: www.lpr-journal.org) Top panel: Two-photon photoemission intensity as a function of pump-probe delay for different intermediate state energies $E - E_F$ in an epitaxial Cu film on Si(111) of 44 nm thickness. A pump pulse of photon energy $h\nu_1 = 2.35$ eV and probe pulse $h\nu_2 = 2h\nu_1 = 4.70$ eV was used. Bottom panel: Hot electron relaxation times as a function of intermediate state energy for different film thicknesses as indicated; reprinted with permission from [50].

Such a finding can be explained by two decay channels and $1/\tau = 1/\tau_{e\text{-}e} + 1/\tau_{transp}$. The transport contribution becomes more important with an increasing film thickness. It is found to be sizeable as it lowers the decay times by 100 fs at the lowest studied energy of 200 meV above E_F. A separation of e-e scattering and transport effects was realized because (i) the 2PPE detection is local and occurs at the surface and (ii) the semiconducting Si substrate exhibits a band gap. Therefore, carriers that propagate according to their momentum $\hbar k$ into the bulk of the film or crystal cannot propagate from the film into the substrate due to the band gap [50, 52]. Thereby a spatial separation of detection and relaxation, which is the basis of the assignment of transport effects, is realized. For Cu and other noble metals a further quantitative analysis requires a more sophisticated theoretical investigation. Such can be found in, e. g., [25, 53]. An improved insight on the basis of experimental data was, however, rather limited for these materials.

3.2. Ag/Fe(100)

Ag/Fe(100) is a prototypical metallic quantum well system [54], which is prepared by epitaxial growth of Ag films on a Fe(100) substrate [55]. In general, an electronic quantum well is formed when ultrathin metal films approach a thickness comparable to the electron de Broglie wavelength [54]. Furthermore, it is essential that electrons in the film are confined along the direction normal to the metal film due to the partial, orientational band gap, which originates from a projection of the bulk electronic band structure onto the surface, here Fe(100). In consequence, only specific electron wavevectors are supported along the interface normal direction and the continuous dispersion in a bulk crystal is modified into a series of discrete quantum well sub-bands (QWSs) [54, 56]. This confinement requires well defined reflection at the interface and therefore high quality interfaces with low defect density, which are realized, e. g., in Ag/Fe(001).

The electronic structure of Ag/Fe(100) is characterized by a series of well-defined quantum well states, which point to a strong confinement of the QWS wave function in the Ag film [54, 55]. The binding energies of the occupied and unoccupied QWS are consistently described within a phase accumulation model. In the following, we focus on a time-resolved 2PPE study from Ogawa et al. investigating the quasi-particle lifetimes of the unoccupied QWSs in the region of $E - E_F \approx 1$ eV [55].

The left panel of Fig. 5 shows the observed population decay times for QWSs as a function of excess energy above E_F and the arrows indicate the binding energy of unoccupied QWSs. The lifetimes amount to $4 - 9$ fs for energies of $E - E_F = 1.1 - 1.5$ eV and do obviously not follow the quadratic scaling law expected from Fermi liquid theory. On the other hand, lifetimes of hot electrons measured on a Ag(100) single crystal surface amount to $8 - 15$ fs for the same excess energy range and show the quadratic scaling with respect to the excess energy $\tau \sim (E - E_F)^{-2}$ [55]. This is in accordance with the expected energy dependence of lifetimes in FLT, see right panel of Fig. 5, and the comparison evidences that the decay of electrons excited in unoccupied Ag QWSs proceeds significantly faster than in bulk Ag. Ogawa et al. conclude from the observed deviation from FLT that besides population decay due to e-e scattering in the metal film, electron scattering and electron transport across the Ag/Fe interface present an additional relaxation channel. This additional decay consequently leads to higher scattering rates and shorter lifetimes compared to bulk.

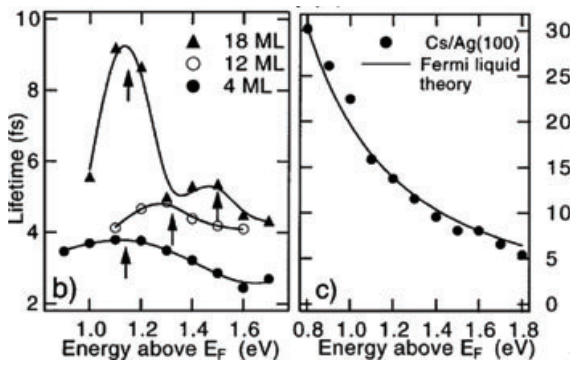

Figure 5 Hot electron lifetimes as function of excess energy for in Ag/Fe(100) for different film thickness given in monolayers (ML) (left) and Ag(100) (right). Note that a submonolayer amount of Cs was adsorbed on the surfaces to lower the workfunction. Arrows indicate the binding energy of unoccupied quantum well states. Reprinted with permission from [55]. Copyright (2002) by the American Physical Society.

This result emphasizes that while the presence of well-defined QWSs indicates electron confinement in the metal film due to the partial band gap of the projected bulk band structure, electron transport across the metal-metal interface is an important contribution to the hot electron lifetimes. Since the projected substrate band gap exists only near the Γ-point scattering of hot electrons into regions of the substrate band structure at larger momenta, where no orientational band gap exists, serves as an important decay channel. In this sense the decay mechanisms at interfaces resemble the decay known for alkali atoms on noble metal surface where elastic decay into the substrate present the essential contribution to explain the observed decay times [25, 57–59].

3.3. Pb/Cu(111)

We now turn to Pb/Cu(111), which presents another example of metallic QWSs on a metal substrate [40]. Mathias and coworkers employ angle-resolved 2PPE to investigate the unoccupied electronic structure and momentum-dependent hot electron dynamics at a coverage of 1 monolayer (ML) Pb/Cu(111), where a single unoccupied QWS is observed at $E - E_F = 2.7$ eV. Like in Ag/Fe(100), the equilibrium electronic structure of 1 ML Pb/Cu(111) is characterized by well-defined QWSs in the occupied and unoccupied density of states, indicative of a high degree of electron confinement.

Fig. 6 shows a color-coded map of the hot electron lifetime in Pb/Cu(111) as function of excess energy $E - E_F$ and the in-plane photoemission angle, which represents the

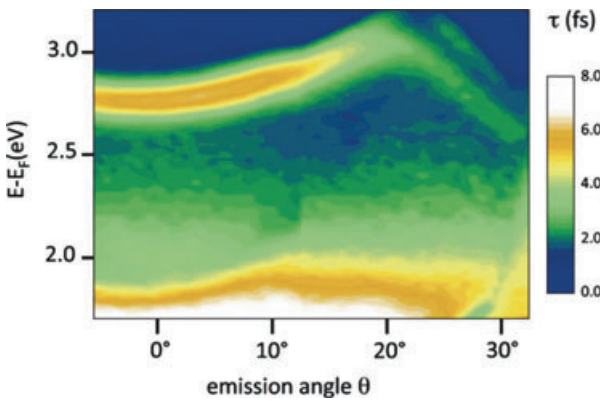

Figure 6 (online color at: www.lpr-journal.org) False color lifetime map as function of excess energy and in-plane electron momentum $k_{||}$ for 1 ML Pb/Cu(111). Reprinted with permission from [40]. Copyright (2010) by the American Physical Society.

in-plane electron momentum $k_{||}$. Mathias and coworkers observe a pronounced momentum dependence of the hot electron lifetimes in the unoccupied QWS. The hot electron lifetimes at the Γ-point amount to 8.4 fs and decrease to 4 fs near the Brillouin zone boundary. These momentum-dependent hot electron lifetimes are explained by the contribution of intra-band scattering events at $k_{||} \neq 0$. In this scenario, electrons excited to finite in-plane momenta relax within the QWS band by means of e-e and e-ph scattering events. The observed electron lifetimes increase towards the band bottom, as seen in Fig. 6, because the electron population near $k_{||} = 0$ is filled by a relaxation of higher lying states at $k_{||} \neq 0$.

Focusing on the lifetimes at the Brillouin zone center, the authors note that the experimentally observed lifetimes of 8.4 fs are 4 fs and 2 fs shorter than expected from FLT for bulk Pb [46] and first principle calculations for Pb/Cu(111) [60], respectively. Mathias et al. suggest that this deviation up to 50% can be explained by electron dynamics in two-dimensional QWS, which could in general be different from three-dimensional bulk materials. The relaxation mechanism at $k_{||} = 0$ remains yet to be investigated. In particular, it will be interesting to distinguish local relaxation in the Pb-adlayer from electron scattering into unoccupied states of the underlying bulk metal, as was the case in Ag/Fe(100).

3.4. $CoSi_2$/Si(111)

In a next step, we turn to metallic quantum well systems on a semiconducting Si(111) substrate and discuss epitaxial $CoSi_2$ films on Si(111) which are grown by depositing Co on a reconstructed Si(111)$-(7\times7)$ surface and subsequent annealing steps [61]. The resulting interface is crystalline and has applications as ohmic or Schottky-type contacts.

Linear and non-linear photoemission reveals that the electronic surface structure of the $CoSi_2$/Si(111) interface near E_F is characterized by a hole-like QWS that is unoccupied near the Γ-point and crosses E_F at finite $k_{||}$ [61]. In contrast to QWS on metallic substrates, this QWS is confined by the global band gap of Si. Near the Γ-point the lowest unoccupied QWS exhibits a binding energy of $E - E_F = 0.65$ eV and thus resides near the Si conduction band bottom of about 0.7 eV. Kutschera and co-workers determine the lifetime of the hot electron population in this state from pump-probe studies to 16(9) fs. This lifetime is in the range expected for a clean Co surface, where hot electron lifetimes at $E - E_F = 0.65$ eV range from $13 - 18(2)$ fs and $17 - 22(2)$ fs for minority and majority carriers in the exchange-split band structure of Co, respectively [53].

Kutschera et al. compare the energy-dependence of the transient 2PPE intensity at energies near the QWS peak. Qualitatively, the hot electron decay proceeds slower in the QWS compared to the electrons measured by the diffuse 2PPE intensity at energies below and above the peak. The quantitative analysis yields a FLT-like quadratic dependence of the hot electron lifetime as function of excess energy $\tau = a(E - E_F)^{-2}$. The prefactor a amounts to 2.2 fs, which

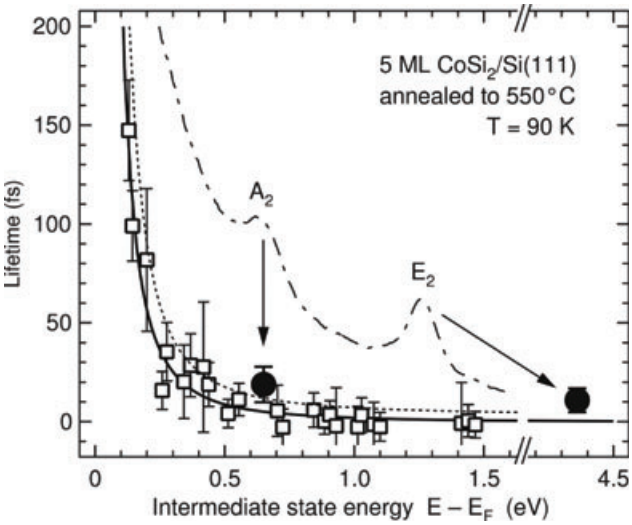

Figure 7 Hot electron lifetimes in $CoSi_2$/Si(111) as function of intermediate state energy. The dashed-dotted line shows the 2PPE intensity for the same energy range and A_2 indicates the position of an unoccupied QWS. Reprinted with permission from [61], published by IOP.

in FLT relates to an electron density of $0.5 \cdot 10^{22}$ cm^{-3}. Compared to elemental bulk metals, where electron densities range from $0.9 \cdot 10^{22}$ cm^{-3} for Cs to $24 \cdot 10^{22}$ cm^{-3} for Be, this particular value seems rather low. Kutschera et al. argue that the hot electron lifetimes are influenced by the high density of states of the Co d-bands below E_F. However, it is difficult to distinguish if the hot electron lifetimes in $CoSi_2$/Si(111) are governed by decay in the film due to e-e scattering and to what extend electron transport across the interface contributes to the lifetimes.

3.5. Pb/Si(111)

Pb/Si(111) is a two-dimensional model system, which has received considerable attention due its well defined interfaces and the resulting high degree of electron confinement that is facilitated by the global Si band gap. This is in contrast to the quasi-degenerate band structures of metal films on metal substrates like Ag/Fe(100).

Pb/Si(111) in particular presents many quantum size effects due to the quantization of the band structure, such as the preference of 'magic' island heights [63], 'devils-staircase' phases [64], oscillations of the critical temperature of the superconducting state [65, 66], of the Hall effect [67] and of the work function [68]. All these properties sensitively depend on the film thickness as the reported oscillation period of 2 ML is directly linked to the modulation of the electron density at $E - E_F$ due to the quantization of the $6p_z$ Pb bulk band [69]. This combination of well-defined interfaces with resulting sharp QWS on a semiconducting substrate makes Pb/Si(111) especially interesting for the study of hot electron dynamics.

Epitaxial Pb films were grown as wedges [70] on a Si(111) surface, resulting in a quasi-continuous thickness

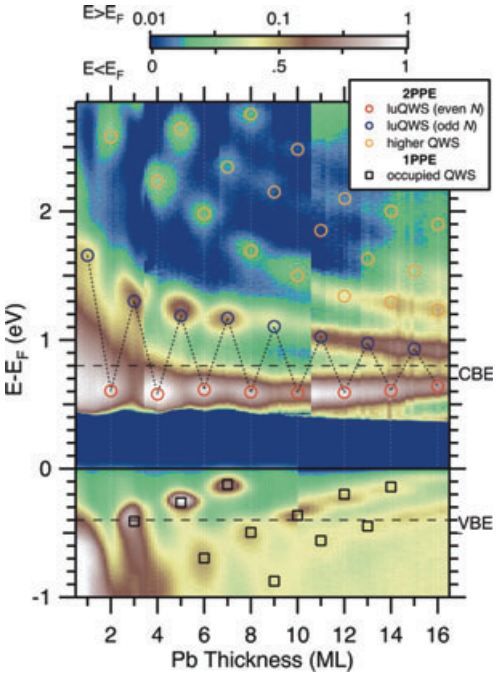

Figure 8 (online color at: www.lpr-journal.org) The false color map of the photoemission intensity of occupied and unoccupied electronic quantum well states (QWSs) in Pb/Si(111) as a function of film thickness has been measured by combining single photon photoemission (1PPE) and 2PPE. The film was prepared as a wedge and moving the laser spot across the thickness gradient sampled a quasi-continuous thickness variation. Line fits of the spectra at constant thickness resulted in the binding energies as indicated by the symbols. The valence and conduction band edge of the Si substrate are indicated by horizontal dashed lines. Note that the energy interval between E_F up to 0.4 eV above E_F is not accessible by the used photon energy; reprinted with permission from [62].

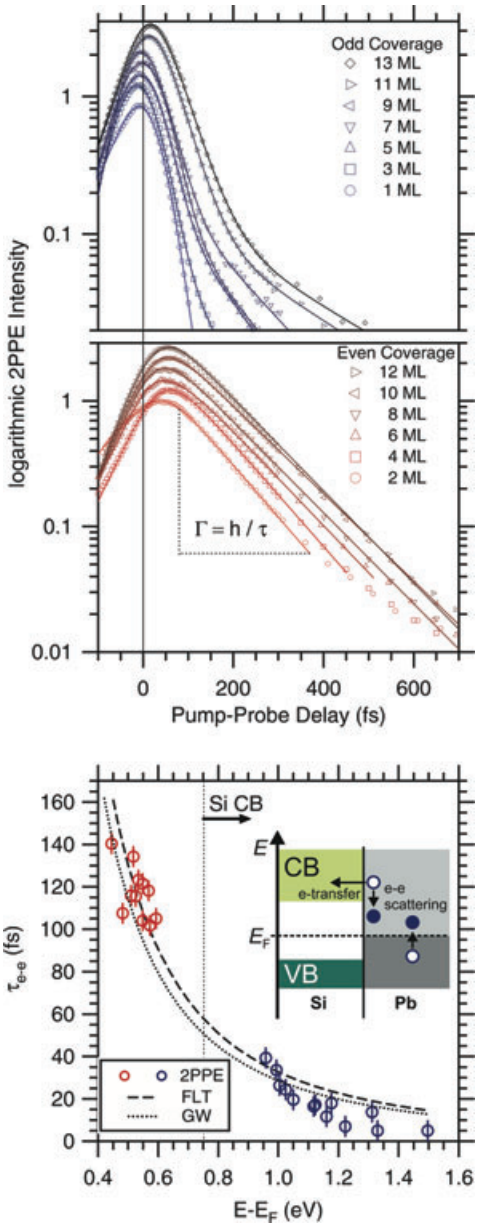

Figure 9 (online color at: www.lpr-journal.org) Time-dependent 2PPE intensity for Pb/Si(111) for odd (even) number of monolayers (ML) in the top (center) panel. The solid lines are fits, which determine the decay times presented in the bottom panel. While decay times of states within the substrate band gap are well described by theoretical predictions according to Fermi liquid theory and the GW *ab initio* approach, the values for states, which are degenerate with the Si conduction band, are smaller than expected theoretically for bare Pb films. The inset indicates how electron transfer to the substrate and e-e scattering within the metal film are competing decay channels for hot electrons; reprinted with permission from [62].

variation [62, 68, 71]. Figure 8 shows the photoemission intensity in a color map as function of Pb film thickness. Occupied states at energies below E_F are probed by one-photon photoemission (1PPE) with a photon energy $h\nu$ larger than the work function $E_F - E_{vac}$ and unoccupied states above E_F by two-photon photoemission (2PPE), where the sum of both photon energies $h\nu_1 + h\nu_2$ is larger than the work function, see Sect. 2. The binding energies of the lowest unoccupied QWSs (luQWSs) oscillate between 1.65 and 0.6 eV for 1 ML thickness variation. The QWS peaks exhibit a high intensity contrast due to an efficient electron confinement to the film at energies of the Si band gap. Hence, the study of electron dynamics of luQWS is especially interesting because it resides in the Si band gap for an even number of ML and thus being confined to the film. In contrast, luQWS is degenerate with Si bands for an odd number of ML.

The top panel of Fig. 9 shows the time domain analysis of the decay of the transient electron population by cross-correlation traces taken at the respective luQWS binding energy as a function of film thickness. For an odd number of ML a very fast population decay is observed, which slows down slightly with increasing thickness. In contrast, for an even number of ML a slower and thickness independent decay is found. The lifetimes are evaluated from a fit of a rate equation model that is convoluted with the laser pulse envelope [71]. Essentially, the lifetimes are given by the

inverse slope of the initial population decay $\tau = \hbar/\Gamma$, as indicated in Fig. 9.

The lifetimes are correlated to the energetic position of the respective luQWS with respect to the Si band gap. If the binding energy of QWS is within the substrate band gap, transport is inhibited and the phase space for e-e- scattering in the film is reduced compared to thickness with a higher binding energy. This is expected to result in longer lifetimes. At energies which are degenerate with the Si conduction band a decay channel due to additional decay by transport into the substrate will be activated and the phase space for e-e scattering will be increased. Both effects lead to shorter relaxation times. Since the luQWS binding energy oscillates with a 2 ML period, characteristic for Pb/Si(111), see Fig. 8, the oscillating binding energies of luQWS might introduce periodic changes in the relaxation time.

To distinguish these limiting cases, the lifetimes are plotted versus the luQWS binding energy in the bottom panel of Fig. 9. As discussed in the beginning of this section, Fermi liquid theory [46, 48] for bulk materials predicts a quadratic scaling law of the inelastic e-e scattering rate $\Gamma_{\text{e-e}} = \hbar/\tau_{\text{e-e}} = a(n) \cdot (E - E_{\text{F}})^2$ as function of the energy above the Fermi level. The measured relaxation times are reproduced on an absolute scale using Fermi liquid theory [48] and employing the electron density n_{Pb} of bulk Pb, which determines the factor $a(n)$ in $\Gamma_{\text{e-e}}$ above. In fact, the Fermi liquid curve may be regarded as a parameter-free description since n_{Pb} depends only on the size of the unit cell and number of valence electrons. This quantitative agreement is a significant improvement compared to earlier studies, presented above.

It is remarkable that despite the two-dimensional character of the thin film band structure [65, 66, 68, 72, 73] the lifetimes are reproduced following the three-dimensional Fermi liquid theory. In addition, the energy dependent lifetimes in bulk Pb from an *ab-initio* calculation employing the GW approximation [25, 74] is shown in Fig. 9 and corroborates the Fermi liquid dependence. We explain this result by the strong screening of the Coulomb interaction in Pb. The Thomas-Fermi screening length of Pb is 0.51 Å due to the rather high electron density in Pb. This value is much smaller than the spatial extension of a single ML, which is 2.86 Å. Therefore, the electron decay rates in Pb/Si(111) are in agreement with predictions for a bulk material albeit ultrathin films have been studied here [62]. We can further conclude that the lifetime oscillations originate from periodic changes in binding energy, which modulate the available phase space for electron decay. Due to the agreement of the experimental and theoretical results we conclude that the lifetimes are (i) dominated by e-e scattering and (ii) follow the Fermi liquid theory for bulk materials.

The above analysis of the hot electron dynamics in Ag/Fe(100) and Cu/Si(111) revealed a sizeable contribution due to transport effects. In Pb/Si(111) a systematic deviation from Fermi liquid theory is only encountered for $E - E_{\text{F}} > 1.2$ eV. We attribute this to an additional decay channel, namely electron transfer into the substrate, because at these energies the states are degenerate with the Si conduction band. These two competing decay channels are illustrated by the inset of Fig. 9.

These results can also help to understand the lifetimes in Ag/Fe(100), which were discussed in Sect. 3.2 and are significantly shorter than in bulk Ag. In this interpretation, the band gap of the surface projected bulk band structure of Ag is sufficient to confine the electronic wave function near the Γ-point and give rise to sharp QWSs. On the other hand, elastic scattering into unoccupied parts of the projected bulk band structure present an additional decay channel for excited electrons which significantly decreases the hot electron decay times. In summary, we have shown that transport contributions to hot electron lifetimes are an essential ingredient for direct comparisons of experimental results and theory. Only if transport channels are blocked the limit described by Fermi liquid theory is reached [62].

4. Many particle dynamics and cooperative effects under non-equilibrium conditions in solid materials

Under the excitation conditions discussed above an interaction of the excited particles was neglected, because their density is too low for a sizeable effect. Through increasing the excitation density to > 0.1 mJ/cm^2 coupling of excited particles becomes essential as shown in the following for quantities like the electron temperature and for a real time description of the occupied electronic band structure that describes the transient non-equilibrium state of the solid.

4.1. Thermalized hot electrons and coupling to lattice vibrations

We start with a discussion of the electron temperature of a photo-excited system and transfer of the energy residing in the electronic subsystem through e-ph coupling to the lattice. As an example we present here results of time-resolved one-photon photoemission for epitaxial metallic films of the lanthanide Gd(0001) with 10-20 nm thickness on a W(110) substrate.

Fig. 10 depicts the time-dependent photoemission intensity in the vicinity of E_{F} in a false color map, see top panel. Photoelectrons are generated in 1PPE by a 4.2 eV probe pulse generated by frequency doubling of the signal output of a VIS OPA. The small work function of Gd(0001), which is below 4 eV, yields a spectrum of more than 0.5 eV width. Optical excitation with the fundamental of the Ti:Sapphire laser at 1.5 eV employing an absorbed pump fluence of 0.4 mJ/cm^2 generates hot electrons far above E_{F}, which are recognized from the intensity increase. Below E_{F} an intensity decrease is found that represents photoexcited holes. At a first glance it appears that these hot carriers decay within about 1.2 ps. Analysis of the respective spectra yield significantly more information. The center panel of Fig. 10 shows selected spectra taken from the intensity map at the given delay times on a logarithmic axis. The top spectrum was

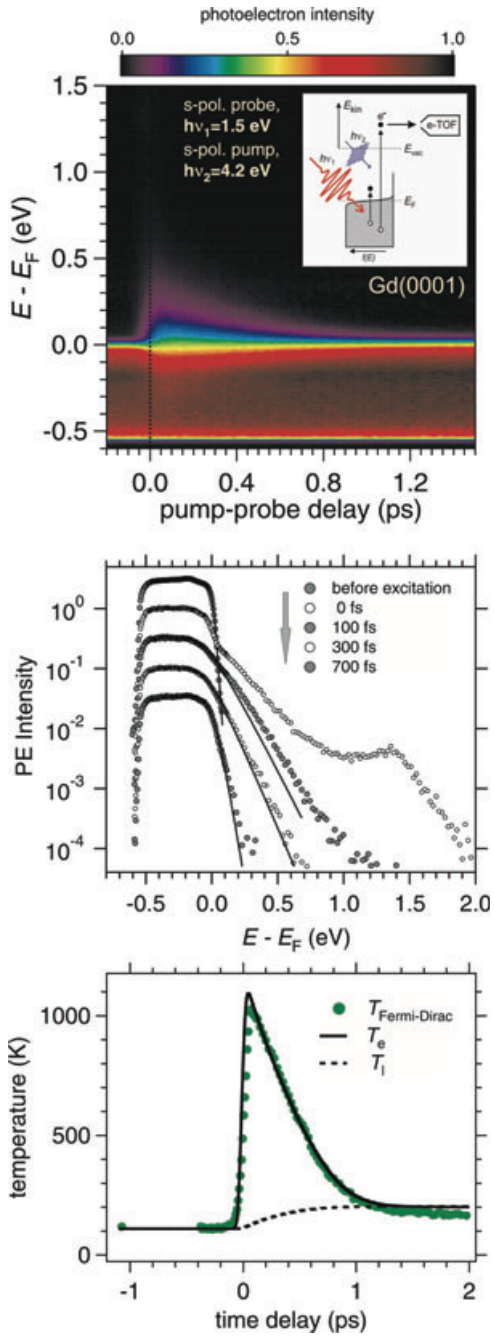

Figure 10 (online color at: www.lpr-journal.org) Top panel: Time-resolved photoelectron intensity depicted as a false color map from epitaxial Gd(0001) films grown on W(110). Photoelectrons were detected in normal emission direction and generated by s-polarized UV probe pulses after excitation by IR pump pulses. The center panel shows the photoelectron spectra around E_F (symbols) on a logarithmic scale for different time delays. The solid lines indicate the thermalized Fermi-Dirac distribution function closest to the respective spectrum. The electron temperature determined from that distribution function is shown in the bottom panel as a function of pump-probe delay (symbols). The solid and dashed line are the results of a simulation of transient electron and lattice temperatures from the two-temperature model; reprinted with permission from [75], published by IOP.

taken before optical excitation. It serves as a reference for the position of E_F. To ensure that determination of the transient electron temperatures is not affected by experimental limitations like, e. g., energy resolution, the spectrum before optical excitation is fitted by a Fermi-Dirac distribution function. This yields the equilibrium temperature in agreement with the independently measured temperature.

The spectrum during optical excitation, taken at optimum pump-probe overlap, i. e. 0 fs delay, shows the photo-excited electrons directly. They appear up to energies $E - E_F = 1.5$ eV because they are generated by absorption of one pump photon. The spectrum cannot be described by a Fermi-Dirac distribution, in particular due to the kink that occurs at E_F in the logarithmic representation. But already after 100 fs the spectrum looks very similar to a thermalized distribution function, which is depicted for reference by a solid line. At delays ≥ 300 fs the spectrum can be reasonably well described by a Fermi-Dirac distribution and the electron system can be considered as internally thermalized. To achieve this, numerous e-e scattering events took place among excited and non-excited carriers, but also interaction of excited carriers plays a role to achieve the thermalized distribution function.

The electron temperatures determined from fitting the Fermi-Dirac distributions to the time-resolved spectra result in the time-dependence of the electron temperature T_e plotted in the bottom panel of Fig. 10. It starts from the equilibrium value of 100 K, peaks near 1000 K, and relaxes to an intermediate level near 200 K. Its time-dependent behavior can be described by the two temperature model that considers an instantaneous increase in T_e and energy transfer to phonons leading to an increase in the lattice temperature T_l by e-ph coupling [77–80]. We find that the two-temperature model describes the transient electron temperature reasonably well, albeit there are deviations immanent in the simplified model during the optical excitation. Therefore one can conclude on the behavior of T_l, which is indicated by the solid line, that after 1.4 ps both transient temperatures have equilibrated.

Before we proceed to the surface dynamics we mention two aspects that are not discussed in depth but are nevertheless worth noting in the present context. First, Gd, which is a ferromagnet, was also investigated regarding its magnetization dynamics. It was found that the magnetization does neither follow simply T_e or T_l. The time-dependent magnetization exhibits a quasi-equilibrium contribution with a time constant of 40 ps and a non-equilibrium one. The latter is linked to the presence of hot electrons [81, 82]. Second, the fact that the two-temperature model describes the electron and lattice dynamics well should be generalized with care. For Ru(0001) we have shown that a competition between energy transfer from electrons to phonons with ballistic transport leads to sizeable deviations from a transient thermalized electron distribution function and that the two-temperature model has to be modified for a successful description [80].

The Gd(0001) surface features a surface state of $5d_{z^2}$ symmetry, which is exchange-split due to the intra-atomic exchange interaction with the magnetic moment of the lo-

calized $4f^7$ electrons and is spin-polarized below the Curie temperature of 293 K. The dynamics of the surface state and its spin-polarization driven by optical excitation was investigated extensively by pump-probe experiments employing optical second harmonic generation (SHG) [83–85] and time-resolved photoemission [86] of the occupied and unoccupied surface state component.

In addition to features that describe excitation and relaxation of the system by means of (non-) thermalized carrier distributions a pronounced coherent dynamic was observed. By coherent we mean that an oscillatory behavior was found, that contains a phase relation with respect to the instant of optical excitation. Such a coherent contribution was detected in the pump-induced changes in SHG intensities [83], but also in, e.g, the surface state binding energy, as presented in the following.

To become sensitive to the Gd(0001) surface state in the time-resolved photoemission experiments the probe pulse polarization was switched from *s*- to *p*-polarized in order to generate a photoelectron yield from the surface state [87]. The respective time-resolved photoelectron spectra are shown by a false color plot in Fig. 11, top panel. Before optical excitation the respective photoemission line is found at a binding energy of $E_B = 180$ meV. Note that here an occupied surface state is probed in 1PPE. After optical excitation, the binding energy is reduced and the line broadens within 1 ps. Since the respective time-dependencies follow the increase in T_e and/or T_l, these pump-induced changes were explained by incoherent dynamics, i. e. heating and energy transfer between electrons and phonons [76]. In addition, a weak intensity modulation can be encountered in the false color map of Fig. 11. An analysis of the variation of the binding energy E_B with time delay facilitates separation of the coherent and incoherent contributions. As depicted in the center panel (A) of Fig. 11 we detect a continuous decrease in E_B from 180 meV before excitation to 140 meV at a delay of 2 ps. The respective time constant follows the increase in T_l according to the two-temperature model. This heating contribution was subtracted from the originally measured $E_B(\Delta t)$ which gives the oscillatory contribution δE_B shown in panel (B) of Fig. 11. This coherent contribution contains a damped oscillation at 3 THz frequency and 2 meV amplitude [76]. The observed frequency is in agreement with a surface phonon derived from a bulk LO-phonon [83] and is coupled to magnetic excitations [84]. Assuming an equilibrium potential the real space amplitude of the vibration has been estimated to 1 pm by translation of the equilibrium change in E_B due to compression of atoms in the surface plane towards the bulk into the time-domain [76].

More recently, such coherent signatures have been observed by time-resolved photoemission for various systems [88–90] and bear the potential of further insight into interaction of electrons with lattice vibrations. In the following, we present a time-resolved ARPES investigation of a model system for charge density wave formation, where the collective excitation modes after ultrafast optical laser excitation are analyzed.

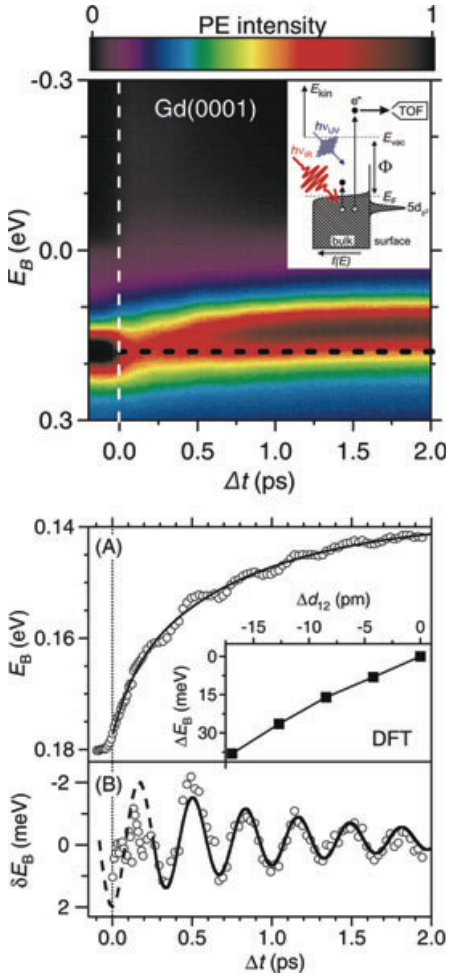

Figure 11 (online color at: www.lpr-journal.org) Top panel: Time-resolved photoelectron intensity in normal emission depicted as a false color map from epitaxial Gd(0001) films. Contrary to Fig. 10 *p*-polarized UV probe (6 eV) and IR pump (1.5 eV) pulses were employed. In this configuration the occupied component of the $5d_{z^2}$ surface state on Gd(0001) results in a pronounced photoemission line. As a function of time delay a binding energy change and line width broadening is observed. The change in binding energy is given in the bottom panel. An incoherent variation attributed to surface heating and a coherent contribution representing an oscillation of the surface layer with a frequency of 3 THz; reprinted with permission from [76], published by IOP.

4.2. Response of a charge density wave material to optical excitation

A charge density wave (CDW) is a broken symmetry ground state with spatially modulated electron and ion densities. It forms at low temperatures in low-dimensional materials with high densities of states at E_F due to an enhanced electron susceptibility at E_F and strong e-ph coupling. Figure 12 depicts the principle of CDW formation. The upper panel shows a one-dimensional atomic chain with period a that forms a half-filled and thus metallic band. Below the CDW phase transition temperature T_{CDW} a spontaneous lattice distortion can double the periodicity to $2a$ and open new band

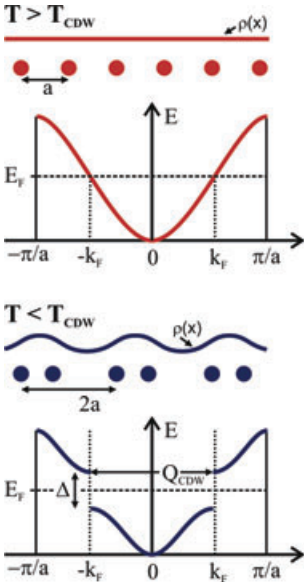

Figure 12 (online color at: www.lpr-journal.org) The top panel depicts a one-dimensional atomic chain with period a that forms a half-filled and thus metallic band with a Fermi momentum of $k_F = \pi/2a$ and a spatially uniform electron density $\rho(x)$. The lower panel schematically shows that below the CDW phase transition temperature T_{CDW} a spontaneous lattice distortion, which doubles the periodicity to $2a$, opens new band gaps Δ at k_F. The Fermi surface nesting by a vector $Q_{CDW} = 2k_F$ thus results in a spatial modulation of $\rho(x)$; after [91].

gaps Δ at k_F, which results in a spatially modulated electron density $\rho(x)$. In general, the driving force of this coupled electron-lattice instability is the minimization of the system's total energy due to a reduction of the kinetic electron energy by opening of a band gap at the Fermi surface. The band gap is a consequence of the lattice modulation with an appropriate wave vector Q_{CDW} that nests parts of the Fermi surface.

In the following we discuss the ultrafast response of the prototypical CDW material $TbTe_3$, which is a member of the RTe_3 family of compounds that exhibit a Fermi surface nesting driven CDW formation [93, 94].

The top panel in Fig. 13 shows a Fermi surface map of $TbTe_3$ in thermal equilibrium for $T = 100$ K, which is far below the CDW phase transition temperature of $T_{CDW} = 335$ K [92]. The data was acquired with synchrotron-based ARPES at SSRL (Stanford, USA) employing a photon energy of 23 eV. The Fermi surface exhibits a characteristic diamond-shaped topology above T_{CDW} (dotted lines), whereas the CDW band gap extends throughout a significant part of the Brillouin zone below T_{CDW}. The nesting vector Q_{CDW} is indicated by a white arrow. The red arc indicates positions along which the tr-ARPES data were taken [89].

We now focus on the dynamics of the CDW state at k_F in the nesting region, as indicated by a red dot in the upper panel, and show the transient photoemission intensity for $T = 100$ K at $k = k_F$ as function of pump-probe delay in Fig. 13b. A pump photon energy of 1.5 eV and a probe photon energy of 6.0 eV was used. At negative pump-probe delays, i. e. before the arrival of the pump pulse, the spectrum exhibits two occupied electronic states. The upper state at a binding energy of $E - E_F \approx -0.25$ eV is identified as the CDW band, which is derived from in-plane $5p_x$ and $5p_z$ Te orbitals [94, 95]. Due to the opening of the CDW band gap at 100 K this state does not disperse through E_F, compare to Fig. 12. The lower band at $E - E_F \approx -0.5$ eV, however, does not contribute to the CDW formation.

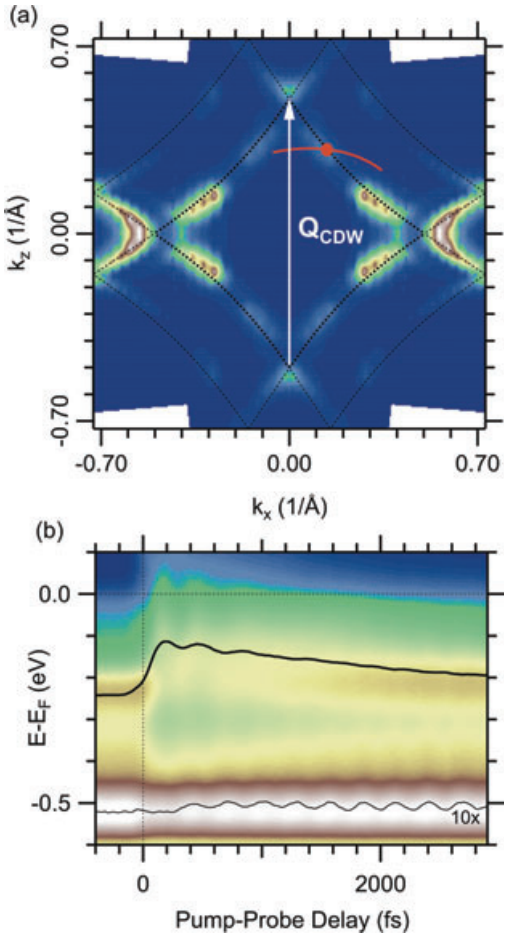

Figure 13 (online color at: www.lpr-journal.org) (a) Fermi surface map of the CDW material $TbTe_3$ at 100 K far below the CDW phase transition temperature of $T_{CDW} = 335$ K [92] where the charge density wave order melts. These ARPES measurements were carried out at a synchrotron light source. The large gapped regions in the Fermi surface originate from the CDW order formed by nesting of particular regions of the Fermi surface by the indicated nesting vector Q_{CDW}. (b) Time-dependence of the direct photoemission intensity at pump fluence of $F = 2.6\,\mathrm{mJ/cm^2}$ taken at an emission angle that corresponds to the Fermi momentum k_F as indicated by a red dot in the upper panel. Two occupied electronic states exhibit oscillations as a function time delay. Center-of-mass analysis (Lorentzian line fits) results in the transient binding energy as indicated by the bold (thin) line. The binding energy changes of the lower band are shown ten-fold increased for visibility; reprinted with permission from [89].

The CDW band responds strongly to the optical excitation by a shift of the spectral weight towards E_F, which is accompanied by the observation of hot electrons above E_F. Compared to the upper CDW band, the lower band exhibits a negligeable shift of the spectral weight. An oscillatory behavior of binding energy, line width and amplitude are nevertheless observed in both electronic states.

The time-dependent spectral function is further analyzed by Lorentzian line fits and center of mass analysis as indicated in Fig. 13b by lines. Fourier transformation and sinu-

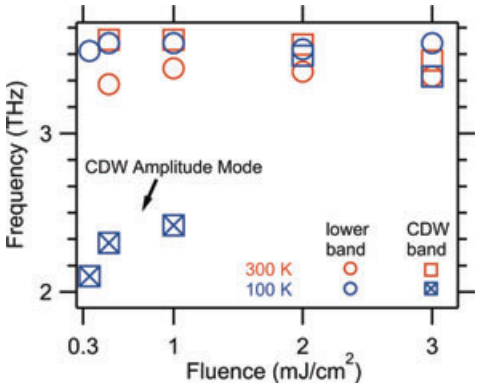

Figure 14 (online color at: www.lpr-journal.org) Coherent oscillation frequencies as a function of excitation density. Squares (circles) indicate frequencies observed in the CDW (lower) band; reprinted with permission from [89].

soidal fits of the transient binding energies yield the oscillation frequencies of the coherent modes, which are shown in Fig. 14 as function of incident pump fluence and temperature. The lower band exhibits a single coherent mode at ~ 3.5 THz, which is largely independent of temperature and excitation density. We thus conclude that the binding oscillations of the lower band originate from the excitation of a generic coherent phonon of $TbTe_3$, as discussed e. g. in [83, 96, 97].

In contrast, the coherent response of the CDW band depends strongly on temperature and fluence: At 300 K, i. e. near the CDW phase transition temperature, as well as at high fluences and 100 K a frequency of ~ 3.5 THz is observed in the CDW band, which is comparable to the mode of the lower band. Interestingly, at low fluences ($F < 1\,\mathrm{mJ/cm^2}$) and a temperature of 100 K, well below T_{CDW}, a new mode with $2.1 - 2.4$ THz is resolved. This mode is intimately connected to the CDW phase since it is observed only in the CDW band below the CDW phase transition temperature, only for electron momenta in the CDW nesting region, and only for low excitation densities, where the charge ordering is not destroyed. Thus, this low frequency mode is assigned to the amplitude mode of the CDW state. Optical excitation of electron-hole pairs constitutes a photo-doping of the electronic part of the CDW, which projects the system on an excited state potential energy surface. This results in a force acting on the ion cores, i. e. the ionic part of the CDW, and initiates a periodic motion of the ion cores [75]. In analogy to the equilibrium CDW physics discussed in Fig. 12, this ion motion leads to modulations of the CDW amplitude. In turn, the CDW amplitude modulates the CDW band gap, which is observed directly here.

The melting of the charge ordered electronic band structure can be monitored in a very direct manner by changing the photoemission angle in the pump-probe experiment. In Fig. 15 we show the photoemission intensity as function of binding energy and electron momentum (indicated by the red arc in Fig. 13) for intense optical excitation at selected delays. Before arrival of the pump pulse, the band dispersion of the CDW band is characterized by the CDW band gap at

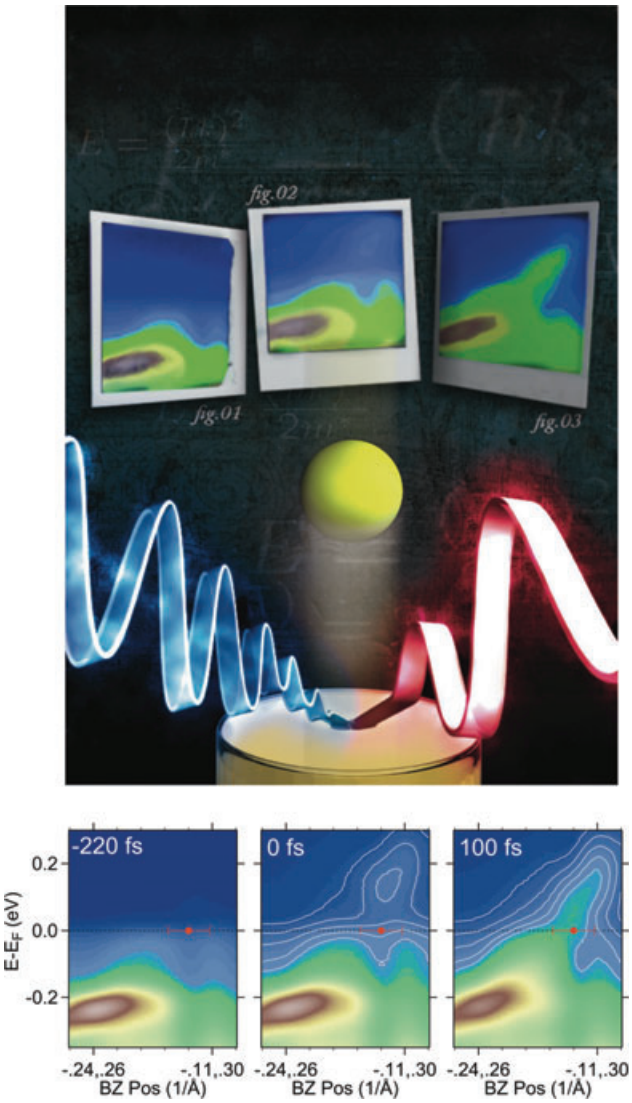

Figure 15 (online color at: www.lpr-journal.org) Energy and momentum dependent photoemission intensity for different time delays before, during, and after optical excitation with $F = 2\,\mathrm{mJ/cm^2}$ in the vicinity of the Fermi momentum k_{F}, which is indicated by red points. Intense optical excitation populates unoccupied states near $E - E_{\mathrm{F}} = 100$ meV close to k_{F}. At a delay of 100 fs the melting of the charge density wave has led to a continuous electronic band indicating a photo-induced closing of the electronic band gap of the low temperature electronic band structure. The contour lines emphasize the population of bands above E_{F}. The top panel shows an artist's view of the tr-ARPES experiment. Data are reprinted with permission from [89].

k_{F}, marked by red dots. Directly at zero pump-probe delay, the occupied band structure remains essentially unchanged but the optical excitation transiently populates a state at $E - E_{\mathrm{F}} \approx 0.2$ eV, indicating the photo-doping of the system due to electron-hole pair excitation. After 100 fs the CDW band gap has closed and the dispersion of the CDW band resembles a nearly-free electron band. Due to scattering of hot electrons into the CDW band its dispersion can be followed well above E_{F}.

This analysis of the CDW model system $TbTe_3$ highlights how the collective coupling of electronic excitations to bosonic degrees of freedom such as lattice motions can be studied directly in the time domain yielding direct insight into the underlying fundamental interaction. The momentum-dependent analysis was essential to distinguish a phonon that represents a particular excitation of the ordered CDW state from a more generic vibrational excitation.

4.3. Electron dynamics at larger electron momenta

The previous section has highlighted the rich physics of momentum dependent electron dynamics that can be expected in strongly correlated materials. One of the experimental issues in applying tr-ARPES to the study of the dynamics at high electron momenta, e. g., near the boundary of the Brillouin zone, is the limited photon energy of ≤ 7 eV, which can be generated in non-linear optical crystals. On the one hand side this results in a small kinetic energy of photoelectrons which limits the access to the center of the first Brillouin zone. On the other hand side the low UV photon energy can lead to unfavorable photoemission cross sections and inhibits probing of core-levels.

One approach to overcome these limitations is high harmonic generation (HHG) in polarizable gas targets [6, 7, 9, 11]. Such HHG sources can provide photon energies of several 10 eV with pulse durations in the range of few 10 fs. Note that with that approach also attosecond time-resolved experiments were realized [7]. Several laboratories have recently demonstrated experiments on solid surfaces employing time-resolved photoelectron spectroscopy using VUV or XUV radiation generated by high harmonic generation [8, 10, 11, 98–100]. This clearly underlines the future impact of this method. However, these setups currently face a limit in the dynamic range of the spectra and energy resolution. This limit is determined by the number of photoelectrons that can be detected per laser pulse before space charge effects occur and therefore by the laser repetition rate of a few kHz. Currently, these sources are limited in their repetition rate to a few kHz due to the requirement of several 100 µJ pulse energy of the driving IR laser.

In the following we discuss a recent example of a tr-ARPES study employing such a HHG generation process of VUV light pulses. Rohwer et al. investigated the CDW material $1T$-$TiSe_2$ using the output of a hollow-core fiber HHG source operating at 3 kHz and 43 eV VUV photon energy with an overall time resolution of 30 fs [11]. We expect that this result will trigger further investigations using related approaches and that time-resolved experiments of such kind will be a widely employed future application of photoelectron spectroscopy.

$1T$-$TiSe_2$ is a layered di-chalcogenide compound exhibiting a CDW phase transition below $T_{CDW} = 200$ K in which the unit cell forms a commensurate $2 \times 2 \times 2$ reconstruction. This doubling of the real space unit cell leads to a characteristic back-folding of the electronic band structure with half the periodicity in k-space similar to Fig. 12. For $T > T_{CDW}$ the band structure near the Γ-point is dominated by the hole-like dispersing Se $4p$ band and an electron pocket with Ti $3d$ character at the M-point zone boundary, corresponding to $k_{||} \approx 1$ Å^{-1}. For $T < T_{CDW}$, the Brillouin zone is reduced to half so that the back-folded Se $4p$ band is observed at the M-point, see Fig. 16b. This back-folding of the electronic bands due to the CDW transition thus allows monitoring crystal structure changes, which are reflected in the electronic structure.

In general, Fig. 16 shows the evolution of the band structure as function of energy and electron momentum for selected pump-probe delays. Note that in their experiment Rohwer et al. are able to monitor a remarkably large portion of the Brillion zone ranging from -0.2 Å^{-1} to 1.2 Å^{-1} without change of the experimental geometry by virtue of the 43 eV photon energy in combination with an imaging-type hemispherical electron energy analyzer, which analyzes photoelectrons regarding kinetic energy and photoemission angle simultaneously. In more detail, Fig. 16 depicts the evolution of photoemission intensity as function of binding energy near E_F and in-plane electron momentum $k_{||}$ for selected pump-probe delays at an incident pump fluence of 5 mJ/cm^2. Panel (b) shows the electronic band structure of the CDW state in equilibrium before optical pumping. The spectrum near the Γ-point is dominated by the Se $4p$ bands. Near the M-point, the hole-like dispersing feature is identified as the back-folded Se $4p$ band, which, however, is superimposed on an electron-like band stemming from Ti $3d$ orbitals. This Ti $3d$ band is not affected by the CDW transition.

At time zero a laser-assisted photoemission (LAPE) signal is observed near Γ, arising from absorption of an IR pump photon by an electron that has already been photoemitted, see Fig. 16c. Since these are free electrons above the vacuum level, they do not exhibit a population decay and the LAPE signal reflects the cross-correlation of pump and probe beams. The electron dynamics near the M-point has two contributions. First, the Ti $3d$ band is transiently populated by hot electrons, resulting in an electron-like band dispersion that can be followed well above E_F. Second, the intensity of the back-folded Se $4p$ band decreases as the system is driven out of the CDW state by the optical excitation. At 30 fs, the back-folded Se band has vanished, indicating that the CDW state has been destroyed and the corresponding reconstruction has been lifted, see Fig. 16d. After 3 ps, the intensity in the Ti band has decayed as the electronic excess was transferred to phonons. This correlates with a partial reappearance of the back-folded Se bands near the M-point, see Fig. 16e.

In principle, measurements of the system's response to the optical excitation should allow to distinguish several microscopic mechanisms that could result in the CDW melting in $1T$-$TiSe_2$. A first limiting case is that the phase transition follows a Peierls-like CDW mechanism involving nesting of parts of the Fermi surface and a displacement of the ion cores into the $2 \times 2 \times 2$ superstructure. In this limit, the fastest response time is given by $\tau_{CDW} = 1/(4\nu)$, where ν is the frequency of the CDW amplitude mode. This is because the heavy ion cores have to move to new equilibrium

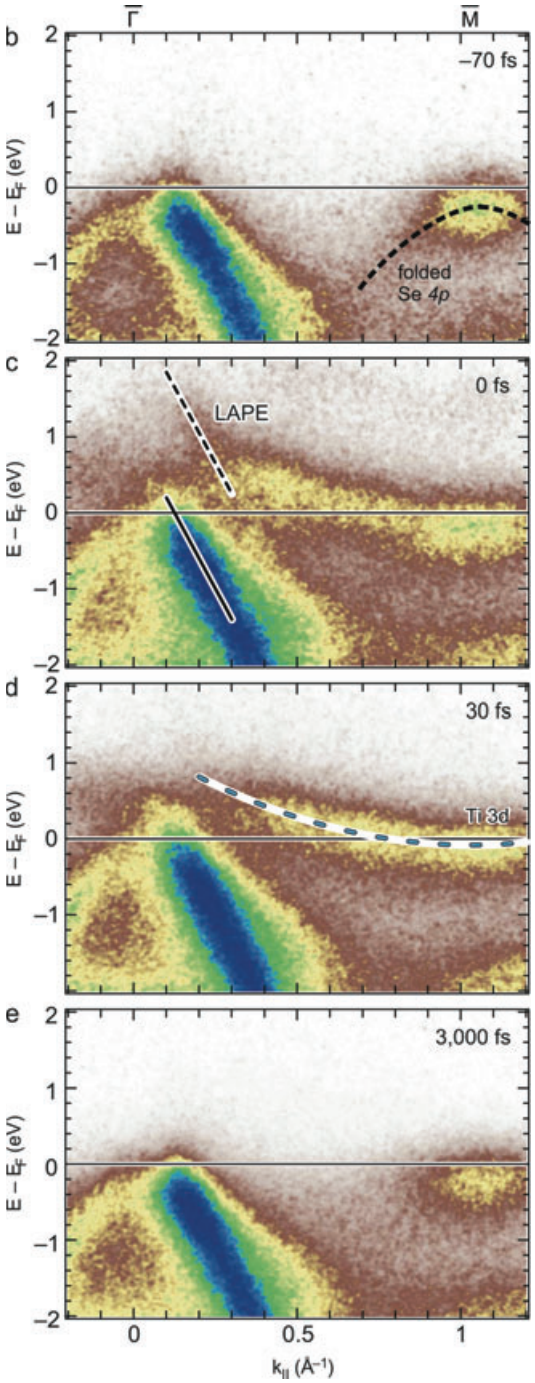

Figure 16 (online color at: www.lpr-journal.org) Time-resolved ARPES intensity of 1*T*-$TiSe_2$ as function of binding energy and in-plane electron momentum for selected pump-probe delays. LAPE (Laser-assisted photoemission) indicates the signal from above-threshold-photoemission, which is used to determine the temporal pump-probe overlap. Reprinted with permission from [11].

positions and the respective time scale experiences a lower bound set by the phonon mode involved. A second limiting case is the concept of an excitonic metal-to-insulator transition. Consider a semiconductor or semimetal with a small band gap ΔE_G, where thermal excitations lead to a finite population of electrons and holes in the conduction and valence band respectively. If the exciton binding energy is larger than ΔE_G, the electronic system will be unstable towards the condensation of excitons as this lowers the systems total energy and opens up a band gap at E_F. In this scenario, the fastest response time is determined by the exciton binding energy, which can be estimated from the transition temperature and the energy uncertainty principle.

For 1*T*-$TiSe_2$, these two timescales can be inferred independently from other measurements and result in $\tau_{CDW} = 75$ fs for a Peierls-like mechanism and $\tau_{ex} = 35$ fs for the excitonic scenario. Comparing these expectations to the time-resolved data shows that with increasing fluence the response is clearly faster than expected from the frequency of the CDW amplitude mode. On the other hand, at the highest fluences 1*T*-$TiSe_2$ responds within 20 fs and thus even faster than given by τ_{ex}.

The authors conclude that the time-limiting step for the optically induced insulator-to-metal transition is given by the time scale of electronic screening in the system. This interpretation allows to quantitatively explain the fluence dependence of the initial drop time, which follows a $1/\sqrt{n}$ dependence, where n is the excited carrier density. This result emphasizes that while the fastest time scales have been thought to be associated with collective excitation modes of system, non-equilibrium processes - like a quasi-instantaneous change of screening - can exceed this limit and open new pathways for, e. g., ultrafast switching devices.

5. Conclusions and Oultlook

In this review we have shown that femtosecond time-resolved non-linear (two-photon) photoelectron spectroscopy is highly sensitive to the decay of hot electrons at interfaces and in metallic layers with thicknesses of several monolayers. Furthermore, time-resolved linear (or one-photon) photoemission allows studying collective phenomena such as coherent phonons by periodic variations in the occupied part of the band structure. For a number of model systems these techniques have led to a detailed understanding of the elementary scattering processes and fundamental interactions that underlie the relaxation of optically excited states.

By investigating metallic layers of Cu and Pb on metallic and semiconducting substrates a competition of spatial redistribution of the electron population by transport effects with local relaxation through e-e scattering was revealed. For a quantum well system realized by epitaxially grown Pb films on Si(111) it was possible to explain the hot electron decay times as function of monolayer film thickness by the rather simple Fermi liquid theory. A quantitative agreement of the Fermi liquid theory with the experimentally determined decay times was obtained for states within the Si band gap. This is in contrast to metallic films on metallic substrates as shown for Ag/Fe(100), where the presence of final states at finite in-plane momenta presents an additional decay channel for elastic scattering across the interface. In general, as was demonstrated for the case of Pb/Si relaxation of states in the film that are degenerate with states of

the substrate, a competition between local e-e scattering in the film and electron transfer across the interface has to be taken into account. Moreover, relaxation of hot electrons also occurs by e-ph coupling. Cooling of a hot electron temperature leads to lattice heating, i. e. excitation of incoherent phonons. Coupling to coherent phonons as discussed for Gd(0001) surfaces or in the CDW material $TbTe_3$ causes a periodic variation of the electron binding energy of the electronic state interacting with that particular mode. For the CDW material $TbTe_3$ time- and angle-resolved photoelectron spectroscopy led to a direct identification of a collective mode of the charge-ordered state. The use of HHG light sources extends the accessible electronic states to the full Brillouin zone. The CDW material $1T$-$TiSe_2$ serves as an example where an optically induced, transient change of the lattice periodicity was monitored through the respective unfolding of the electronic band structure in real-time. These experiments are sensitive to the coupling of certain electronic states to specific boson modes. This aspect makes the tr-ARPES technique very promising for future studies as it reveals the energy and momentum dependence of the electron-boson coupling, which is one key ingredient for the understanding of the emergence of low symmetry ground states in solid materials.

Independent of the already demonstrated capabilities it will be important to realize shorter pulses for a wider range of wavelengths, which will provide access to high frequency modes beyond 10 THz [21]. For such short pulses the band width of the pulses limits the energy resolution in time-resolved spectroscopy. As demonstrated by attosecond spectroscopy from solid surfaces a spectral separation can still be achieved for suitable problems like separation of different bands [98]. Nevertheless, we believe that the novel information obtainable in the time domain will outweigh the loss in spectral resolution. In general, control of the time-band width product, allowing a mutual optimization of energy and time resolution for a given problem, will very likely become an essential issue.

We alluded to the different excitation densities required to realize investigations of (i) the decay of electron populations by few particle decay and (ii) coupling to bosonic modes at considerably higher excitation density. In the latter regime excited particles interact with each other leading to non-equilibrium distribution functions and many-body effects that govern the dynamics.

As the experimental finesse progresses, novel theoretical concepts are under development that aim at describing the non-equilibrium state and provide essential complements to the experimental findings. Established theoretical approaches include the *GW* approximation [74] for calculating excited electron lifetimes, solving the Bethe-Salpeter equation [101] to understand the coupling of molecular degrees of freedom to hot electrons and time-dependent wave packet propagation, and density matrix calculations for photochemical dynamics. New, promising approaches towards the description of the transient spectral function are the extension of established mean field theories into the time domain [31, 102–104] as well as time-dependent functional theory [105] to solve the quantum many-body problem.

Acknowledgements. We acknowledge the excellent support we received over the last decade. This work has been funded by the Deutsche Forschungsgemeinschaft and in part by the US Department of Energy. We are in particular grateful to Martin Wolf and to the Freie Universität Berlin for continuous support of the activities. This work was only possible because of our coworkers and collaborators, who shared the excitement on ultrafast processes with us. We wish to thank G. Bihlmayer, S. Blügel, E. V. Chulkov, C. Gahl, M. Lisowski, P. A. Loukakos, R. G. Moore. L. Perfetti, L. Rettig, F. Schmitt, V. M. Silkin, Z.-X. Shen, J. Stähler, and X. Zubizarreta.

Received: 10 November 2010, **Revised:** 11 September 2011, **Accepted:** 22 November 2011

Published online: 13 February 2012

Key words: Photoelectron spectroscopy, ultrafast dynamics, low dimensional systems, femtosecond lasers.

Patrick Kirchmann obtained his Ph. D. degree in Physics in 2009 from the Freie Universität Berlin, Germany for his experimental work on ultrafast electron dynamics in low-dimensional solid state materials. During his postdoctoral stay from 2009 to 2011 in the group of Z.-X. Shen in Stanford he set up a time-resolved photoemission experiment for material science and collaborated on time-resolved X-ray diffraction experiments at the Linear Coherent Light Source. He received a Feodor-Lynen Fellowship from the Alexander-von-Humboldt Foundation in 2010. Since 2011 he is leading the Dynamics of Correlated Materials group at the Fritz Haber Institute of the Max Planck Society in Berlin, Germany.

Uwe Bovensiepen received his Ph. D. degree in physics in 2000 from the Freie Universität Berlin, Germany, for his experimental work on phase transitions in ultrathin ferromagnetic film systems. In 2000, he worked as a postdoc at the Fritz-Haber Institute, where he started femtosecond time-resolved experiments at interfaces. In 2001 he moved to the Freie Universität Berlin where he set up a femtosecond laboratory to investigate ultrafast dynamics in solids and at interfaces in the group of Martin Wolf. He received his habilitation in 2005 and was supported by a Heisenberg fellowship of the DFG afterwards. In 2009 he was appointed as a full professor at the University of Duisburg-Essen.

References

[1] S. Hüfner, Photoelectron spectroscopy, Springer series in solid-state science, Vol. 82 (Springer, Berlin, 1995).
[2] A. Damascelli, Z. Hussain, and Z. X. Shen, Rev. Mod. Phys. **75**, 473 (2003).
[3] Koralek, J. F. Douglas, N. C. Plumb, Z. Sun, A. Fedorov, M. M. Murnane, H. C. Kapteyn, S. T. Cundiff, Y. Aiura,

K. Oka, H. Eisaki, and D. S. Dessau, Phys. Rev. Lett. **96**, 017005 (2006).
[4] T. Kiss, F. Kanetaka, T. Yokoya, T. Shimojima, K. Kanai, S. Shin, Y. Onuki, T. Togashi, C. Zhang, C. T. Chen, and S. Watanabe, Phys. Rev. Lett. **94**, 057001 (2005).
[5] R. Haight, Surf. Sci. Rep. **21**, 275 (1995).
[6] T. Haarlammert and H. Zacharias, Curr. Opin. Solid State Mater. Sci. **13**, 13 (2009).
[7] F. Krausz and M. Ivanov, Rev. Mod. Phys. **81**, 163 (2009).
[8] S. Mathias, M. Bauer, M. Aeschlimann, L. Miaja-Avila, H. Kapteyn, and M. Murnane, in: Time-resolved photoelectron spectroscopy at surfaces using femtosecond XUV-pulses, edited by U. Bovensiepen, H. Petek, and M. Wolf, Dynamics at solid state surfaces and interfaces Vol. 1 (Wiley-VCH, Weinheim, 2010).
[9] M. Bauer, C. C. Lei, K. Read, R. Tobey, J. Gland, M. M. Murnane, and H. C. Kapteyn, Phys. Rev. Lett. **87**, 0255001 (2001).
[10] L. Miaja-Avila, G. Saathoff, S. Mathias, J. Yin, C. La o vorakiat, M. Bauer, M. Aeschlimann, M. M. Murnane, and H. C. Kapteyn, Phys. Rev. Lett. **101**(4), 046101 (2008).
[11] T. Rohwer, S. Hellmann, M. Wiesenmayer, C. Sohrt, A. Stange, B. Slomski, A. Carr, Y. Liu, L. Miaja Avila, M. Kalläne, S. Mathias, L. Kipp, K. Rossnagel, and M. Bauer, Nature **471**, 490 (2011).
[12] P. Drude, Ann. Phys. **1**, 566 (1900).
[13] H. Petek and S. Ogawa, Prog. Surf. Sci. **56**, 239 (1997).
[14] A. Mokhari, P. Cong, J. L. Herek, and A. H. Zewail, Nature **348**, 225 (1990).
[15] A. Assion, M. Geisler, J. Helbing, V. Seyfried, and T. Baumert, Phys. Rev. A **54**, R4605 (1996).
[16] M. F. Emde, A. Baltuska, A. Kummrow, M. S. Pshenichnikov, and D. A. Wiersma, Phys. Rev. Lett. **80**, 4645 (1998).
[17] K. Ishioka and O. V. Misochko, in: Coherent lattice oscillations in solids and their optical control, edited by K. Yamanouchi, A. Giulietti, and K. Ledingham, Progress in Ultrafast Intense Laser Science Vol. 5 (Springer, Berlin, 2010), pp. 23–63.
[18] J. Shah, Ultrafast Spectroscopy of Semiconductors and Semiconductor Nanostructures, 2nd edn. (Springer, Berlin, 1983).
[19] T. Kampfrath, L. Perfetti, F. Schapper, C. Frischkorn, and M. Wolf, Phys. Rev. Lett. **95**, 187403 (2005).
[20] D. Song, F. Wang, G. Dukovic, M. Zheng, E. D. Semke, L. E. Brus, and T. F. Heinz, Phys. Rev. Lett. **100**, 225503 (2008).
[21] S. Wall, D. Prabhakaran, A. T. Boothroyd, and A. Cavalleri, Phys. Rev. Lett. **103**, 097402 (2009).
[22] J. Hong and D. L. Mills, Phys. Rev. B **62**, 5589 (2000).
[23] R. Vollmer, M. Etzkorn, P. S. A. Kumar, H. Ibach, and J. Kirschner, Phys. Rev. Lett. **91**, 147201 (2003).
[24] M. Weinelt, A. B. Schmidt, M. Pickel, and M. Donath, Prog. Surf. Sci. **82**, 388 (2007).
[25] E. V. Chulkov, A. G. Borisov, J. P. Gauyacq, D. Sanchez-Portal, V. M. Silkin, V. P. Zhukov, and P. M. Echenique, Chem. Rev. **106**, 4160 (2006).
[26] A. Mönnich, J. Lange, M. Bauer, M. Aeschlimann, I. A. Nechaev, V. P. Zhukov, P. M. Echenique, and E. V. Chulkov, Phys. Rev. B **74**, 035102 (2006).
[27] U. Bovensiepen, H. Petek, and M. Wolf, Dynamics in Solid States Surfaces and Interfaces, Vol. 1, Current Developments (Wiley-VCH, Weinheim, 2010).
[28] A. Föhlisch, P. Feulner, F. Hennies, A. Fink, D. Menzel, D. Sanchez-Portal, P. M. Echenique, and W. Wurth, Nature **436**, 373 (2005).
[29] F. Schwabl, Quantum mechanics (Springer, Berlin, 1992).
[30] R. A. Marcus and N. Sutin, Biochim. Biophys. Acta **811**, 265 (1985).
[31] M. Eckstein and M. Kollar, Phys. Rev. B **78**, 245113 (2008).
[32] A. Borisov, S. Sánchez-Portal, R. Díez Muiño, and P. M. Echenique, Chem. Phys. Lett. **387**, 95 (2004).
[33] J. Fraxedas, J. Trodahl, S. Gopalan, L. Ley, and M. Cardona, Phys. Rev. B **41**, 10068 (1990).
[34] B. A. McDougall, T. Balasubramanian, and E. Jensen, Phys. Rev. B **51**, 13891 (1995).
[35] T. Valla, A. V. Fedorov, P. D. Johnson, and S. L. Hulbert, Phys. Rev. Lett. **83**, 2085 (1999).
[36] M. Weinelt, J. Phys.: Cond. Mat. **14**, R 1099 (2002).
[37] N. H. Ge, C. Wong, and C. Harris, Acc. Chem. Res. **33**, 111 (2000).
[38] T. Fauster and W. Steinmann, in: Two-photon photoemission spectroscopy of image states, edited by P. Halewi, Electromagnetic Waves: Recent Developments in Research Vol. 2 (Elsevier, Amsterdam, 1995), p. 347.
[39] J. Güdde, M. Rohleder, and U. Höfer, Appl. Phys. A **85**, 345 (2006).
[40] S. Mathias, A. Ruffing, F. Deicke, M. Wiesenmayer, M. Aeschlimann, and M. Bauer, Phys. Rev. B **81**, 155429 (2010).
[41] J. Güdde and U. Höfer, Prog. Surf. Sci. **80**, 49 (2005).
[42] J. Güdde, M. Rohleder, T. Meier, S. W. Koch, and U. Höfer, Science **318**, 1287 (2007).
[43] J. Lindhard, Dan. Mat.-fys. Medd. **28**, 2 (1954).
[44] P. C. Becker, H. L. Fragnito, C. H. B. Cruz, R. L. Fork, J. E. Cunningham, J. E. Henry, and C. V. Shank, Phys. Rev. Lett. **61**, 1647 (1988).
[45] R. Huber, F. Tauser, A. Brodschelm, M. Bichler, G. Abstreiter, and A. Leitenstorfer, Nature **414**, 286 (2001).
[46] J. J. Quinn and R. A. Ferrell, Physical Review **112**(3), 812 (1958).
[47] D. Pines and P. Nozieres, The Theory of Quantum Liquids (Benjamin, New York, 1966).
[48] G. F. Giuliani and G. Vignale, Quantum Theory of the Electron Liquid (Cambridge University Press, Cambridge, UK, 2005).
[49] S. D. Brorson, J. G. Fujimoto, and E. P. Ippen, Phys. Rev. Lett. **59**, 1962 (1987).
[50] M. Lisowski, P. A. Loukakos, U. Bovensiepen, and M. Wolf, Appl. Phys. A **79**, 739 (2004).
[51] E. Knoesel, A. Hotzel, and M. Wolf, Phys. Rev. B **57**, 12812 (1998).
[52] M. Aeschlimann, M. Bauer, S. Pawlik, R. Knorren, G. Bouzerar, and K. H. Bennemann, Appl. Phys. A **71**, 485 (2000).
[53] R. Knorren, K. H. Bennemann, R. Burgermeister, and M. Aeschlimann, Phys. Rev. B **61**, 9427 (2000).
[54] T. C. Chiang, Surface Science Reports **39**, 181 (2000).
[55] S. Ogawa, H. Nagano, and H. Petek, Phys. Rev. Lett. **88**, 116801 (2002).
[56] M. Milun, P. Pervan, and D. P. Woodruff, Rep. Prog. Phys. **65**, 99 (2002).
[57] A. G. Borisov, J. P. Gauyacq, A. K. Kazansky, E. V. Chulkov, V. M. Silkin, and P. M. Echenique, Phys. Rev. Lett. **86**, 488 (2001).

[58] M. Bauer, S. Pawlik, and M. Aeschlimann, Phys. Rev. B **60**, 5016 (1999).
[59] H. Petek, M. J. Weida, H. Nagamo, and S. Ogawa, Science **288**, 1402 (2000).
[60] A. Zugarramurdi, N. Zabala, V. M. Silkin, A. G. Borisov, and E. V. Chulkov, Phys. Rev. B **80**, 115425 (2009).
[61] M. Kutschera, T. Groth, C. Kentsch, I. L. Shumay, M. Weinelt, and T. Fauster, J. Phys.: Condens. Matter **21**, 134006 (2009).
[62] P. S. Kirchmann, L. Rettig, X. Zubizarreta, V. M. Silkin, E. V. Chulkov, and U. Bovensiepen, Nature Physics **6**, 782 (2010).
[63] Z. Zhang, Q. Niu, and C. K. Shi, Phys. Rev. Lett. **80**, 5381 (1998).
[64] M. Hupalo, J. Schmalian, and M. C. Tringides, Phys. Rev. Lett. **90**, 216106 (2003).
[65] Y. Guo, Y. F. Zhang, X. Y. Bao, T. Z. Han, Z. Tang, L. X. Zhang, W. G. Zhu, E. G. Wang, Q. Niu, Z. Q. Qiu, J. F. Jia, Z. X. Zhao, and Q. K. Xue, Science **306**, 1915 (2004).
[66] S. Qin, J. Kim, Q. Niu, and C. K. Shih, Science **324**, 1314 (2009).
[67] I. Vilfan, M. Henzler, O. Pfennigstorf, and H. Pfnür, Phys. Rev. B **66**, 241306 (2002).
[68] P. S. Kirchmann, M. Wolf, J. H. Dil, K. Horn, and U. Bovensiepen, Phys. Rev. B **76**, 075406 (2007).
[69] C. Wei and Y. Chou, Phys. Rev. B **66**, 233408 (2002).
[70] R. K. Kawakami, E. Rotenberg, H. J. Choi, E. J. Escorcia-Aparicio, M. O. Bowen, J. H. Wolfe, E. Arenholz, Z. D. Zhang, N. V. Smith, and Z. Q. Qiu, Nature **398**, 132 (1999).
[71] P. S. Kirchmann and U. Bovensiepen, Phys. Rev. B **78**, 035437 (2008).
[72] M. H. Upton, C. M. Wei, M. Y. Chou, T. Miller, and T. C. Chiang, Phys. Rev. Lett. **93**(2), 026802 (2004).
[73] Y. F. Zhang, J. F. Jia, T. Z. Han, Z. Tang, Q. T. Shen, Y. Guo, Z. Q. Qiu, and Q. K. Xue, Phys. Rev. Lett. **95**, 096802 (2005).
[74] P. M. Echenique, R. Berndt, E. V. Chulkov, T. Fauster, A. Goldmann, and U. Höfer, Surf. Sci. Rep. **52**, 219 (2004).
[75] U. Bovensiepen, J. Phys.: Cond. Matter **19**, 083201 (2007).
[76] P. A. Loukakos, M. Lisowski, G. Bihlmayer, S. Blügel, M. Wolf, and U. Bovensiepen, Phys. Rev. Lett. **98**, 097401 (2007).
[77] S. I. Anisimov, B. L. Kapeliovich, and T. L. Perel'man, Sov. Phys. JETP **39**, 375 (1974).
[78] P. B. Allen, Phys. Rev. Lett. **59**, 1460 (1987).
[79] J. Hohlfeld, S. S. Wellershoff, J. Güdde, U. Conrad, V. Jähnke, and E. Matthias, Chem. Phys. **251**, 237 (2000).
[80] M. Lisowski, P. A. Loukakos, U. Bovensiepen, J. Stähler, C. Gahl, and M. Wolf, Appl. Phys. A **78**, 165 (2004).
[81] A. Melnikov, H. Prima-Garcia, M. Lisowski, T. Gießel, R. Weber, R. Schmidt, C. Gahl, N. M. Bulgakova, U. Bovensiepen, and M. Weinelt, Phys. Rev. Lett. **100**, 107202 (2008).
[82] M. Wietstruk, A. Melnikov, C. Stamm, T. Kachel, N. Pontius, M. Sultan, C. Gahl, M. Weinelt, H. Dürr, and U. Bovensiepen, Phys. Rev. Lett. **106**, 127401 (2011).
[83] A. Melnikov, I. Radu, U. Bovensiepen, O. Krupin, K. Starke, E. Matthias, and M. Wolf, Phys. Rev. Lett. **91**, 227403 (2003).
[84] A. Melnikov, I. Radu, A. Povolotskiy, T. Wehling, A. Lichtenstein, and U. Bovensiepen, J. Phys. D: Appl. Phys. **41**, 164004 (2008).
[85] A. Melnikov and U. Bovensiepen, in: Coherent Excitations at Ferromagnetic Gd(0001) and Tb(0001) Surfaces, edited by U. Bovensiepen, H. Petek, and M. Wolf, Dynamics at solid state surfaces and interfaces Vol. 1 (Wiley-VCH, Weinheim, 2010).
[86] M. Lisowski, P. A. Loukakos, A. Melnikov, I. Radu, L. Ungureanu, M. Wolf, and U. Bovensiepen, Phys. Rev. Lett. **95**, 137402 (2005).
[87] M. Wolf, A. Hotzel, E. Koesel, and D. Velic, Phys. Rev. B **59**, 5926 (1999).
[88] L. Perfetti, P. A. Loukakos, M. Lisowski, U. Bovensiepen, H. Berger, S. Biermann, P. S. Cornaglia, A. Georges, and M. Wolf, Phys. Rev. Lett. **97**, 067402 (2006).
[89] F. Schmitt, P. Kirchmann, U. Bovensiepen, R. G. Moore, L. Rettig, M. Krenz, J. H. Chu, N. Ru, L. Perfetti, D. H. Lu, M. Wolf, I. Fisher, and Z. X. Shen, Science **321**, 1649 (2008).
[90] L. Rettig, R. Cortes, S. Thirupathaiah, P. Gegenwart, H. S. Jeevan, M. Wolf, J. Fink, and U. Bovensiepen, Phys. Rev. Lett. , in press, available at http://arxiv.org/abs/1110.3938.
[91] G. Grüner, Density Waves in Solids, Frontiers in Physics, Vol. 89 (Addison-Wesley, 1994).
[92] N. Ru, C. L. Condron, G. Y. Margulis, K. Y. Shin, J. Laverock, S. B. Dugdale, M. F. Toney, and I. R. Fisher, Phys. Rev. B **77**, 035114 (2008).
[93] E. DiMasi, M. C. Aronson, J. F. Mansfield, B. Foran, and S. Lee, Phys. Rev. B **52**, 14516 (1995).
[94] R. G. Moore, V. Brouet, R. He, D. H. Lu, N. Ru, J. H. Chu, I. R. Fisher, and Z. X. Shen, Phys. Rev. B **81**, 073102 (2010).
[95] V. Brouet, W. L. Yang, X. J. Zhou, Z. Hussain, R. G. Moore, R. He, D. H. Lu, Z. X. Shen, J. Laverock, S. B. Dugdale, N. Ru, and I. R. Fisher, Phys. Rev. B **77**, 235104 (2008).
[96] O. V. Misochko, K. Ishioka, M. Hase, and M. Kitajima, J. Phys.: Condens. Matter **18**, 10571 (2006).
[97] M. Hase, K. Ishioka, J. Demsar, K. Ushida, and M. Kitajima, Phys. Rev. B **71**, 184301 (2005).
[98] A. L. Cavalieri, N. Müller, T. Uphues, V. S. Yakovlev, A. Baltuska, B. Horvath, B. Schmidt, L. Blümel, R. Holzwarth, S. Hendel, M. Drescher, U. Kleineberg, P. M. Echenique, R. Kienberger, F. Krausz, and U. Heinzmann, Nature **449**, 1029 (2007).
[99] H. Dachraoui, M. Michelswirth, P. Siffalovic, P. Bartz, C. Schäfer, B. Schnatwinkel, J. Mattay, W. Pfeiffer, M. Drescher, and U. Heinzmann, Phys. Rev. Lett. **106**, 107401 (2011).
[100] J. C. Petersen, S. Kaiser, N. Dean, A. Simoncig, H. Y. Liu, A. L. Cavalieri, C. Cacho, I. C. E. Turcu, E. Springate, F. Frassetto, L. Poletto, S. S. Dhesi, H. Berger, and A. Cavalleri, Phys. Rev. Lett. **107**, 177402 (2011).
[101] M. Rohlfing and S. G. Louie, Phys. Rev. B **62**, 4927 (2000).
[102] J. K. Freericks and V. V. Zlatic, Rev. Mod. Phys. **75**, 1333 (2003).
[103] M. Eckstein, M. Kollar, and P. Werner, Phys. Rev. Lett. **103**, 056403 (2009).
[104] B. Moritz, T. P. Devereaux, and J. K. Freericks, Phys. Rev. B **81**(16), 165112 (2010).
[105] E. Runge and E. K. U. Gross, Phys. Rev. Lett. **52**, 997 (1984).